

Effect of a Combined Hot-Streak and Swirl Profile on Cooled 1.5-Stage Turbine Aerodynamics: An Experimental and Computational Study

Maxwell G. Adams

Department of Engineering Science,
University of Oxford,
Parks Road,
Oxford OX1 3PJ, UK
e-mail: max@maxadams.com

Paul F. Beard

Department of Engineering Science,
University of Oxford,
Parks Road,
Oxford OX1 3PJ, UK
e-mail: paul.beard@eng.ox.ac.uk

Mark R. Stokes

Rolls-Royce plc,
Derby DE24 8BJ, UK
e-mail: mark.stokes@rolls-royce.com

Fredrik Wallin

GKN Aerospace Engine Systems,
SE-461 81 Trollhättan, Sweden
e-mail: fredrik.wallin@gknaerospace.com

Kam S. Chana

Department of Engineering Science,
University of Oxford,
Parks Road,
Oxford OX1 3PJ, UK
e-mail: kam.chana@eng.ox.ac.uk

Thomas Povey¹

Department of Engineering Science,
University of Oxford,
Parks Road,
Oxford OX1 3PJ, UK
e-mail: thomas.povey@eng.ox.ac.uk

Recently developed lean-burn combustors offer reduced NO_x emissions for gas turbines. The flow at exit of lean-burn combustors is dominated by hot streaks and residual swirl, which have been shown—individually—to impact turbine aerodynamic performance. Studies have shown that residual swirl at inlet to the high-pressure (HP) stage predominantly affects the vane aerodynamics, while hot streaks affect the rotor aerodynamics. Studies have also shown that these changes to the HP stage aerodynamics can affect the downstream intermediate-pressure (IP) vane aerodynamics. Yet, to date, there have been no published studies presenting experimental turbine test data with both swirl and hot streaks simultaneously present at inlet. This paper presents the first experimental and computational investigation into the effects of combined hot streaks and swirl on turbine aerodynamics. Experimental measurements were conducted in the Oxford Turbine Research Facility (OTRF), a short-duration rotating transonic facility, in which the nondimensional parameters relevant to turbine fluid mechanics and heat transfer are matched to engine conditions. The turbine under investigation is the recently commissioned LEMCOTEC turbine, which has been designed to represent modern aero-engine architectures and for robustness to lean-burn combustor-representative inlet flows. The turbine comprises an unshrouded HP stage with fully film-cooled vanes followed by low-turning IP vanes in an S-shaped duct. Two turbine inlet flows are considered. The first is uniform in total pressure, total temperature, and flow angle. The second features a nonuniform total temperature (hot streak) profile featuring strong radial and weak circumferential variation superimposed on a swirling velocity profile. This combined nonuniform profile is generated using a new combustor simulator that has recently been commissioned in the OTRF. Detailed area surveys of the flow were conducted at turbine inlet, HP rotor exit, and IP vane exit, and loading distributions were measured on the HP and IP vanes. Measurements and unsteady Reynolds-averaged Navier–Stokes (URANS) predictions suggest that the inlet temperature nonuniformity was relatively well preserved upon being convected through the turbine: the predicted root-mean-square variation in the IP vane exit total temperature field was approximately double that with uniform inlet conditions. Relatively poor comparisons between URANS and experiment highlight the challenge of accurately predicting the complex IP vane flow. In particular, small differences in exit whirl angle resulted in substantial differences in IP vane exit velocity and thus radial pressure gradient. [DOI: 10.1115/1.4049103]

Keywords: computational fluid dynamics (CFD), fluid dynamics and heat transfer phenomena in compressor and turbine components of gas turbine engines

Introduction

Civil aero-engine manufacturers are shifting toward the use of lean-burn combustors in order to reduce environmentally harmful NO_x emissions that arise at high combustion temperatures. However, the flow exiting lean-burn combustors is highly nonuniform and this can cause problems for the downstream turbine. Lean-burn combustors aggressively swirl the combustion air in order to enhance fuel-air mixing and reduce peak temperatures. Residual swirl persists downstream of the combustion zone and presents at turbine inlet. Coolant air is introduced through the combustor liner, causing strong radial temperature gradients near the endwalls,

where the coolant flows meet the hot mainstream flow. Comparatively weak circumferential temperature variations arise due to the separated mixing flow structure generated by the discrete swirlers.

Turbine inlet nonuniformities are known to affect turbine aerodynamics, heat transfer, and therefore performance. Experimental data are required to understand the impacts of lean-burn combustors on the high-pressure (HP) and subsequent turbine stages and to validate computational fluid dynamics (CFD) codes. Measurements of these impacts within an engine are made challenging by the harsh flow conditions experienced. This has led to the use of scaled turbine test facilities, such as the Oxford Turbine Research Facility (OTRF), in order to obtain measurements at engine-representative conditions. Developments in combustor simulators for scaled turbine test facilities have enabled several experimental studies, often accompanied by CFD studies, on the effects on the turbine due to hot streaks and swirl individually. Key results from such studies are summarized below.

¹Corresponding author.

Contributed by the Heat Transfer Division of ASME for publication in the JOURNAL OF TURBOMACHINERY. Manuscript received August 5, 2019; final manuscript received September 15, 2020; published online February 1, 2021. Assoc. Editor: Thomas Praisner.

Hot-Streak Effects. In a stationary blade row, the inviscid streamline pattern and Mach number distribution is unchanged by the introduction of inlet density (or temperature) nonuniformities, provided the inlet total pressure distribution is unaltered. This theoretical result is well known as the Munk and Prim Substitution Principle [1], after the authors who first proved it, and has been corroborated by numerous experimental and computational turbine studies (see, for example, Refs. [2,3]).

In the rotor, relatively hot/cold gas migrates circumferentially toward the rotor pressure/suction side (PS/SS) surface, respectively. This effect is explained by the fact that—for a given Mach number—gas with higher static temperature has higher absolute velocity, and as a result, high-temperature gas is associated with higher rotor incidence angle than low-temperature gas. This so-called preferential migration effect was first described by Kerrebrock and Mikolajczak [4] in the context of compressor aerodynamics and has been experimentally and computationally corroborated by several turbine studies (see, for example, Refs. [2,5]).

Streamwise (secondary) vorticity in the rotor is generated by gradients in rotary total pressure and—to a generally smaller degree—density, which arise in the presence of hot streaks. This effect was first described by Hawthorne [6]. The vorticity produced by typical hot streaks (with hotter gas near mid-span and colder gas near the endwalls) has similar sign to the classical secondary flow vortices in the rotor. Furthermore, as the preferential migration effect described above causes hot gas accumulation near the rotor PS, the gradient-induced vorticity is strongest near the PS. The combined effect is that hot gas tends to migrate toward, and radially spread out across, the PS.

Buoyancy forces in the rotor promote radial migration of hot gas toward the hub. This purely inviscid effect was first described by Shang and Epstein [7]. However, as noted by Prasad and Hendricks [5], for viscous flows, the radial migration of the hot-streak in the rotor passage is determined by the relative magnitudes of this buoyancy effect and the gradient-driven secondary flow effect described above. Thus, hot streaks can migrate radially toward either the hub (as observed by Shang and Epstein [7], for example) or casing (as observed by Butler et al. [2], for example).

Over the past two decades, there have been a number of OTRF investigations of the MT1 HP turbine stage with inlet hot streaks ([8–13], [3]), which utilized two generations of hot-streak simulators ([14,15]; see also Ref. [16]). Most recently, Beard et al. [3] measured a reduction in mixed-out stage efficiency of 0.88% compared with the efficiency with uniform inlet conditions. As the vane aerodynamics were unaffected by the hot streak, the efficiency penalty was attributed to increased losses in the rotor, which arose due to off-design incidence and increased gradients in rotary total pressure and density.

Swirl Effects. Over the past decade, there have been a number of OTRF investigations of the MT1 turbine using a combustor simulator producing a lean-burn combustor-representative swirl profile superimposed on a uniform total temperature profile [17].

Qureshi et al. [18] reported the first rotating turbine experiments with inlet swirl. The off-design vane incidence angles associated with the inlet swirl profile caused significant changes in the vane loading distributions near the endwalls and deformation of the leading-edge (LE) stagnation lines; these effects were greatest on the vane whose LE was aligned with the swirler. The vane secondary flow structure was altered by the off-design incidence angles and the propagation of the swirl vortex through the vane. The loss characteristics were also altered: increased/decreased loss was observed in spanwise regions where vane loading was increased/decreased, respectively, and new high/low-loss regions appeared where boundary layer (BL) fluid accumulated/dissipated, respectively, on the vane surfaces and endwalls. The authors highlighted the challenge presented by these changes—in particular, the redistribution of PS surface streamlines on the vane aligned with the swirler—for cooling system design.

A subsequent OTRF study reported by Qureshi et al. [19] investigated effects of swirl on rotor aerodynamics and heat transfer. With swirl, changes to the vane exit yaw angles and total pressure profiles caused changes in rotor-relative incidence angle and total pressure. The changes in rotor incidence angle were consistent in sign with the swirl vortex at vane inlet, although (as expected) the off-design rotor incidence angles were small in comparison to the off-design vane incidence angles as a result of the flow acceleration through the vane. The changes in incidence angle (and hence rotor-relative total pressure) caused changes in blade loading distribution, tip leakage flow structure, and surface streamline pattern.

Beard et al. [20] measured a mixed-out efficiency penalty of 1.22% with swirl. This penalty was primarily attributed to increased loss in the vane, which arose due to off-design incidence (the changes in rotor aerodynamics were small in comparison with the vane).

More recently, Johansson et al. [21] investigated the effects of swirler clocking on the aerodynamics of a low-turning intermediate-pressure (IP) vane downstream of the MT1 HP stage in the OTRF. Results showed clear (but complex) changes in IP vane loading distributions and IP vane exit flow structure, which indicated that the effects of swirl persisted through the 1.5-stage turbine.

Outside of Oxford, the effects of swirl have been investigated using the low-speed large-scale turbine rig at Technische Universität Darmstadt. Experiments have been conducted using a 1.5-stage research turbine with film-cooled HP vanes and endwalls. These studies have focused on the robustness of the endwall cooling system to swirl [22] and on the total pressure losses and vane and endwall coolant migration with swirl [23]. Both studies reported significant reductions in endwall cooling effectiveness with swirl: coolant was redistributed, leaving some surfaces virtually uncooled. In Ref. [23], additional loss cores were observed with swirl; these were attributed to interaction between the swirl vortex and the HP vane (rather than interaction between the swirl vortex and the cooling flows). Similar interactions were reported in the linear cascade study reported by Jacobi et al. [24].

Using the tri-sector lean-burn combustor simulator at the University of Florence [25] with a uniform inlet total temperature profile, Bacci et al. [26] used a pressure-sensitive paint technique to measure HP vane film-cooling effectiveness with inlet swirl. The results highlighted significant effects of swirl on the performance (effectiveness distribution) of the film-cooling system. The LE stagnation line positions, surface streamline patterns, and swirler loss core each played significant roles in determining the coolant coverage on the vane surfaces.

Combined Hot-Streak and Swirl Effects. To date, there have been only two published studies of the effects of combined hot streaks and swirl on a downstream turbine stage, and both were purely computational. The first study, reported by Khanal et al. [27], concluded that the effects of combined hot-streak and swirl profiles at turbine inlet were not well predicted by a simple superposition of their predicted effects when imposed separately. The second study, reported by Rahim and He [28], concluded that the hot-streak migration through the HP vane was significantly altered by the introduction of swirl and, as a result, the vane exit total temperature profile and blade heat transfer characteristics were significantly modified.

Recently, nonrotating (HP vane-only) experiments with combined temperature distortion and swirl, using the tri-sector lean-burn combustor simulator at the University of Florence [25], have been reported by Bacci et al. [29]. The study focused on hot-streak migration through the vane, with swirlers aligned with every second vane LE. The secondary flow structures, total pressure losses, and hot-streak and coolant migration patterns were different in vane passage aligned/misaligned with the swirler. At vane exit, the predominantly radial hot-streak profile remained pronounced and the introduction of vane film coolant increased the degree of circumferential nonuniformity.

Despite the significant progress made through the studies reviewed above, no study published to date has included an experimental investigation of the effects of combined hot streaks and swirl on a rotating turbine. Such an investigation is motivated by the significance of the effects of swirl and hot streaks individually for turbine aerodynamic and cooling system design, and the prediction that these effects do not superimpose linearly.

Experimental Setup

The Oxford Turbine Research Facility. The OTRF is a short-duration wind tunnel capable of matching Mach number, Reynolds number, corrected speed, gas-to-wall temperature ratio, and turbulence intensity to engine conditions. Steady conditions are typically achieved for approximately 400 ms. The operation of the facility was described by Hilditch et al. [30].

For the present investigation, the facility was fitted with the LEMCOTEC 1.5-stage research turbine. The design and commissioning of the LEMCOTEC turbine was reported by Beard et al. [31]. Figure 1 presents vane/blade mid-span sections and a meridional schematic of the annulus line. The turbine comprises a single HP stage featuring 40 fully film-cooled stator vanes and 60 unshrouded flat-tipped rotor blades. Downstream of the HP stage are 20 low-turning IP vanes in an S-shaped duct. This configuration is representative of a modern high-bypass civil aero-engine architecture with counterrotating HP and IP rotors. The design operating conditions of the turbine are listed in Table 1.

Lean-Burn Combustor Simulator. For tests with nonuniform turbine inlet conditions (combined hot-streak and swirl profile), a fully annular lean-burn combustor simulator was installed upstream of the turbine in the OTRF. The design of the simulator is described in Refs. [32,33]. The integration and commissioning of the combustor simulator in the OTRF was described by Adams et al. [34]. During a test run, hot gas is supplied to the turbine inlet through an annular array of 20 discrete swirlers, which are aligned with

Table 1 LEMCOTEC turbine design operating point in the OTRF

Parameter	Nominal value
Re_{HPV}	2.13×10^6
$\Gamma = \dot{m} \sqrt{T_{01}} / p_{01}$	$5.90 \times 10^{-4} \text{ kg s}^{-1} \text{ K}^{1/2} \text{ Pa}^{-1}$
$N / \sqrt{T_{02}}$	390.1 rpm $\text{K}^{-1/2}$
M_2	0.917
p_{01}	8.5 bars
p_{01}/p_3	2.86
p_{03}/p_4	1.37
T_{01}	475 K
T_{01}/T_w	1.64
T_{01}/T_{0c}	1.64
\dot{m}_1 , kg/s	23
$\dot{m}_{c,HPV}/\dot{m}_1$	6.85%

the mid-span LE of every second HP vane. Cold gas is ejected from annular slots at the hub and casing endwalls downstream of the swirlers in order to produce a radial temperature nonuniformity.

As discussed by Adams et al. [34], a significant drop in the hot stream total temperature was measured across the combustor simulator due to convective heat loss to the simulator hardware. This resulted in a mass-mean total temperature at turbine inlet of $\bar{T}_{01} = 446.4 \text{ K}$ (averaged over 20 runs), which is 6.0% below the design value of 475 K. Measurement of this temperature drop was conducted only after completion of the OTRF experimental investigation discussed in this paper and thus \bar{T}_{01} was not exactly matched between tests with uniform and nonuniform conditions. For each individual run at a given condition, \bar{T}_{01} was consistent to within 2%, or less than 10 K, of the average over all runs.

In addition to changes in turbine performance due to the introduction of nonuniform inlet conditions (which would be expected to arise also at matched \bar{T}_{01}), a change in turbine performance due to the reduction in \bar{T}_{01} alone can be expected. This performance change should vary predominantly with corrected speed, $N/\sqrt{T_{02}}$, where N is the turbine rotational speed and \bar{T}_{02} is the mass-mean total temperature at vane exit/rotor inlet (accounting for the HP vane film coolant flow). The measured values of \bar{T}_{01} and corrected speed with uniform and nonuniform inlet conditions (each averaged over 20 runs) are compared in Table 2. With uniform inlet conditions, the corrected speed is well matched to the design value listed in Table 1. With nonuniform inlet conditions, the corrected speed is increased by 3.1%.

Figures 2(a) and 2(b) show the measured profiles of turbine inlet total pressure, p_{01} , and total temperature, T_{01} , respectively. All measured data have been averaged over at least two good test runs. Note that data radially outside of the measured region (20–95% span) have been extrapolated using radial trends from unsteady Reynolds-averaged Navier–Stokes (URANS) predictions of the combustor simulator (circumferentially averaged) fixed to the local measured values at a particular circumferential location at the radial limit of the measured region. Secondary velocity vectors (also extrapolated as described above) superimposed on the p_{01} profile show a vortex core near mid-span, which coincides with a region of low total pressure (high loss due to overturning of the low-momentum fluid). The maximum variation in the p_{01} profile is small at $\pm 0.35\%$. The corresponding radial profiles of

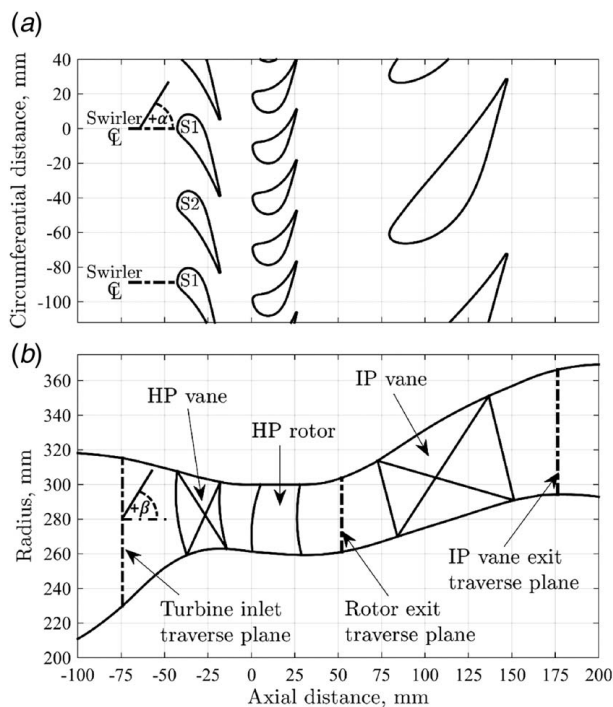


Fig. 1 Schematics of the LEMCOTEC turbine: (a) blade mid-span sections with swirler centerlines and definition of yaw angle, α , indicated and (b) meridional view with traverse planes and definition of pitch angle, β , indicated

Table 2 Experimentally measured mass-mean total temperature at turbine inlet and corrected speed with uniform and nonuniform inlet conditions (each averaged over 20 runs)

Parameter	Uniform inlet	Nonuniform inlet	Difference (non-uniform)
\bar{T}_{01} , K	475.0	446.4	-6.0%
$N / \sqrt{T_{02}}$, rpm $\text{K}^{-1/2}$	389.8	401.7	+3.1%

circumferentially averaged p_{01} and T_{01} are presented in Figs. 2(c) and 2(d). The maximum and minimum values of $T_{01}^{radial}/\bar{T}_{01}$ are 1.090 and 0.842, respectively, where T_{01}^{radial} is the radial (circumferentially averaged) profile. These values are significantly greater than the corresponding values for $T_{01}^{circ}/\bar{T}_{01}$ (maximum 1.058 and minimum 0.996), where T_{01}^{circ} is the circumferential (radially averaged) profile. This quantifies the strength of the radial nonuniformity relative to the circumferential nonuniformity, which for lean-burn combustor exit profiles is typically high.

Figure 2(e) shows the radial profile of circumferentially averaged yaw angle, α_1 (defined in Fig. 1(a)), and Fig. 2(f) shows circumferential profiles of α_1 extracted along constant-span lines at 10%, 50%, and 90% span. These profiles are consistent with a counter-clockwise vortex, as viewed from downstream, entering the vane with peak swirl angles of +30.9 and -28.4 deg.

For tests with uniform inlet conditions, the combustor simulator was replaced with a system of radial rods, which act as passive turbulence generators. Survey measurements of p_{01} and T_{01} confirmed a high degree of uniformity in the turbine inlet flow—see Figs. 2(c)

and 2(d). The measured mass-mean total temperature at turbine inlet was $\bar{T}_{01} = 475.0$ K (averaged over 20 runs), which is in excellent agreement with the design condition.

Measurement Instrumentation. The measurements of the uniform and nonuniform inlet profiles were described by Adams et al. [34]. For measurement of HP vane loading distributions, two HP vanes were instrumented, each with eight pneumatic tapings at 50% and 90% span. Measurements at 10% span were made unfeasible by film-cooling holes and internal feed plenums. For tests with nonuniform inlet conditions, the two instrumented HP vanes were interchanged between runs to obtain measurements at both clocking positions with respect to the swirler. Three IP vanes were instrumented with a total of 107 tapings at 10%, 50%, and 90% span. Due to the blade count ratio of 2:3:1, which coincides with a single combustor pitch, each IP vane experiences an identical flow field and thus the measurements from different vanes can be combined to represent a single vane. Measurements were obtained

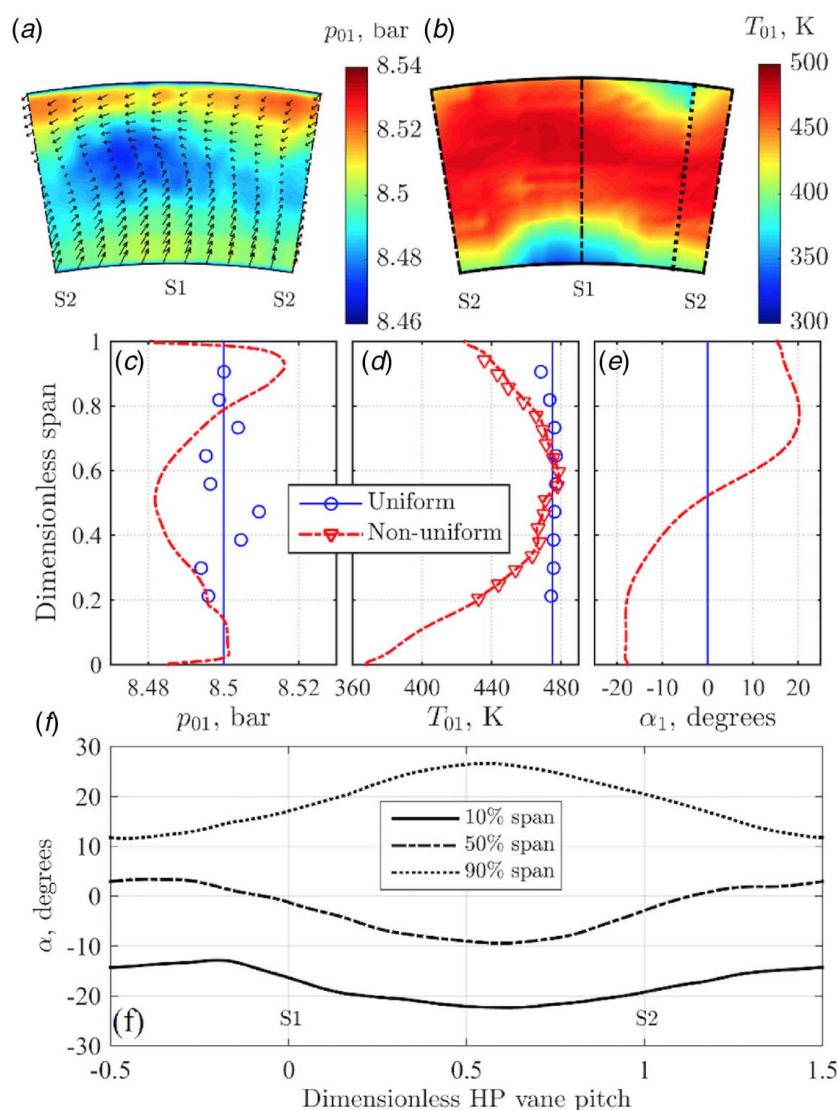


Fig. 2 Turbine inlet profiles. Nonuniform 2D profiles over a single combustor pitch (as viewed from downstream): (a) measured total pressure and predicted secondary velocity vectors and (b) measured total temperature. Measured and predicted uniform and nonuniform radial profiles: (c) total pressure, (d) total temperature, and (e) yaw angle, where markers represent OTRF measurements and lines represent time-averaged URANS predictions. (f) Predicted circumferential profiles of yaw angle at 10%, 50%, and 90% span with nonuniform inlet conditions.

using pressure transducers of range 10 bars and traceable full-scale accuracy of $\pm 0.07\%$.

Area-survey measurements of total temperature were conducted at the rotor-exit traverse plane—see Fig. 1(b)—one axial chord downstream of the rotor blade. For these measurements, a rake of 10 radially distributed aspirated thermocouples (K-type with wire diameter $25.4\ \mu\text{m}$) was used. The rake was stationary during each test run and incrementally shifted between runs to cover a circumferential range of one HP vane pitch (9 deg) with uniform inlet conditions or one combustor simulator pitch (18 deg) with nonuniform inlet conditions. The circumferential resolution was in both cases 0.9 deg. The radial resolution of the survey (set by the spacing of the thermocouples) was 3.9 mm or 9.1% of the duct span at the traverse plane.

Area-survey measurements were also conducted at the IP vane exit traverse plane—see Fig. 1(b)—0.43 axial chords downstream of the IP vane. A traverse probe featuring a three-hole pneumatic probe and two aspirated thermocouples (K-type with wire diameter $25.4\ \mu\text{m}$) was used to measure the steady total pressure, Mach number, yaw angle, and total temperature fields. During each run, the probe was traversed circumferentially at a fixed radial height by a pneumatic actuator coupled to a calibrated linear position sensor. The radial height of the probe was adjusted between runs. The radial resolution of the survey was 3.0 mm or 4.1% of the duct span at the traverse plane, as set by the radial increment (3.1 mm, which is approximately the diameter of the probe tip). The three-hole probe was calibrated over a range of Mach numbers from 0.2 to 1.2 and a range of yaw angles spanning ± 20 deg in a transonic wind tunnel. The calibration technique and uncertainties are reported in Ref. [21]. The circumferential resolution (determined by the transient response of the probe and the traverse speed) was 0.7 deg or 3.7% of an IP vane pitch.

Numerical Setup

Solver and Mesh. Full 1.5-stage URANS simulations were performed using the commercial solver ANSYS CFX. The $k-\omega$ shear stress transport model was used for turbulence closure. The blade count ratio of 2:3:1 permitted a conveniently periodic computational domain covering only 18 deg circumferentially, which corresponds to a single combustor pitch. The same block-structured mesh (~ 19.4 million hexahedral elements) was used for simulations with uniform and nonuniform inlet conditions. Sliding-plane interfaces were used between the stationary/rotating blade rows. The time period over which a rotor blade passes a full combustor pitch was discretized into 240 time-steps. A dual time-stepping method was used with 15 internal iterations to achieve pseudo-steady convergence at each physical time-step. Unsteady simulations were run until temporal periodicity of the solution—as measured for pressure, temperature, and velocity at a number of positions throughout the domain—was observed for at least five passings of a given rotor blade through the domain.

To ensure that the tip clearance in the URANS model was consistent with the experimental geometry, the blade tip clearance was measured in the test facility, while the rotor was at rest, using a feeler gauge. Second, the elongation of the rotor blade in the radial direction during rotation at the design speed was modeled using a finite-element model. Finally, the resulting tip clearance during rotation at the design speed was estimated using the two results and incorporated in the computational mesh.

Boundary Conditions. For simulations with uniform inlet conditions, the turbine inlet total pressure and total temperature profiles were set uniformly at the measured values of 8.5 bars and 475 K, respectively. The yaw and pitch angles at turbine inlet were defined as axial and turbulence intensity was set at 10%, based on hot-wire traverse measurements conducted downstream of the turbulence bars at atmospheric conditions [35].

For simulations with nonuniform inlet conditions, the turbine inlet total pressure, total temperature, yaw angle, and pitch angle distributions were imposed using the measured 2D profiles shown in Fig. 2. In the absence of turbulence measurements at the exit of the combustor simulator in the OTRF, the turbine inlet turbulence intensity was kept at 10% (Beard et al. [20] measured a turbulence intensity of 11.2% downstream of a comparable swirl generator operating in the OTRF). The k and ω properties were imposed uniformly at the domain inlet using the standard ANSYS CFX settings.

For both simulations, an outflow boundary condition (BC) was imposed at IP vane exit using a radial profile of static pressure that varied linearly from hub to casing. The values at the hub and casing were determined by circumferentially averaging measurements from nine static pressure tapings distributed across one IP vane pitch at the same axial location at the domain exit in the URANS model.

Isothermal wall BCs were imposed (at 290 K) at all vane, blade, and endwall surfaces, which approximately represents OTRF conditions during the run. The cavities between the rotor hub platform and the HP/IP vane platforms were crudely modeled using free-slip BCs, while smooth viscous walls were imposed elsewhere.

Film-Cooling Source Term Model. High-pressure vane film cooling was modeled using the source term method described by Nagawkar [36]. For each cooling hole, mass flux with prescribed total temperature, velocity components, and turbulence properties is introduced at a single-cell face closest to position of the real cooling hole. For a given cooling hole mass flowrate, the momentum flux therefore depends on the cell face area. Thus, when generating the mesh, the cell face areas on the HP vane surface were chosen to deliver engine-realistic momentum fluxes. Because the cooling holes and internal plenums were not resolved in the mesh, this source term method permitted reduced cell counts and hence faster computations. The method was verified against CFD results in which the cooling holes and internal plenums were fully resolved (see Ref. [36]).

High-Pressure Vane Aerodynamics

High-Pressure Vane Loading Distributions. The Munk and Prim substitution principle [1] implies that changes to the HP vane loading distribution with nonuniform inlet conditions cannot arise directly from the inlet total temperature nonuniformity. However, changes may arise due to the inlet swirl profile, the (weak) inlet total pressure nonuniformity, and—near the trailing edge (TE)—changes in either the stage operating point or rotor aerodynamics.

Figure 3 presents measurements and URANS predictions of HP vane loading distributions with uniform and nonuniform inlet conditions. Measurements are shown for both cooled and uncooled vanes, while URANS predictions are shown only for cooled vanes. The uncooled-vane measurements were discussed and compared with uncooled steady Reynolds-averaged Navier–Stokes (RANS) predictions by Adams et al. [34] (omitted from Fig. 3 for clarity). All measurements shown have been averaged over at least two good test runs. Where pressure transducers failed, data have been omitted.

With nonuniform inlet conditions, results are shown for vanes at both clocking positions with respect to the swirlers. These clocking positions are denoted as S1 (vane LE aligned with swirler centerline) and S2 (vane LE aligned midway between two swirlers) and are indicated in Fig. 1(a). With uniform inlet conditions, measurements and predictions for both vanes collapsed onto a single trend and thus only data for vane S1 are plotted. All static pressure data have been normalized by the mass-mean total pressure at turbine inlet. Experimental data have been averaged over at least two OTRF runs; data from different runs were in excellent agreement.

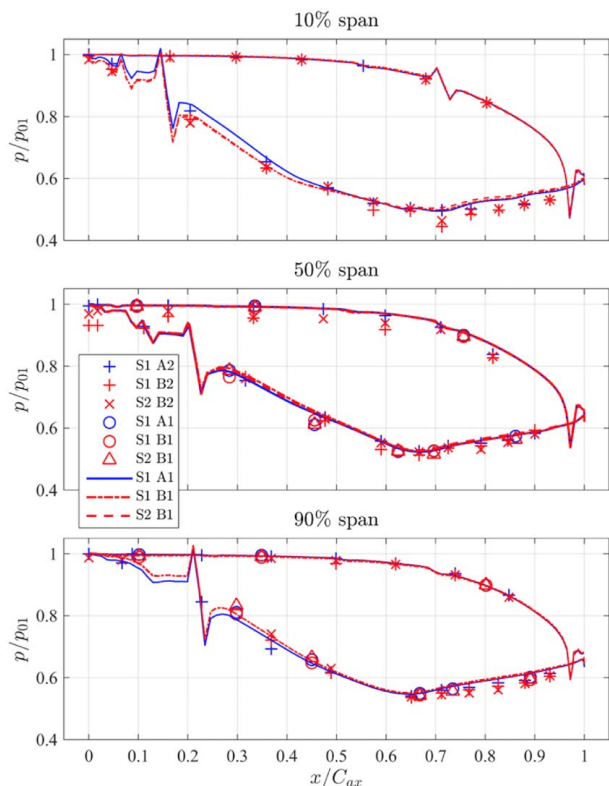


Fig. 3 Measured (markers) and predicted (lines) HP vane loading distributions at 10%, 50%, and 90% span with uniform and nonuniform inlet conditions. Static pressure data have been normalized by normalized by \bar{p}_{01} .

At 10% span (where measurements on cooled vanes were not feasible) the predicted static pressures on the early SS ($x/C_{ax} < 0.5$) of both cooled vanes are reduced (by up to 5.7%) with the introduction of swirl, while little change is predicted elsewhere. This causes increased loading on the forward part of the vane and can be attributed to positive incidence near the hub. The predicted change in vane loading distribution is virtually identical for both vanes, which is consistent with the circumferential yaw angle profile at 10% span (similar values at LE of both vanes)—see Fig. 2(f). The predicted changes (with swirl) in cooled vane loading distributions are consistent with the measurements on the uncooled vanes at 10% span, except for ($x/C_{ax} > 0.7$), where the measured static pressures are up to 10% lower than the predictions. This likely results from a difference in vane throat area between the experimental and CFD geometries (smaller throat area in experiment), as discussed by Beard et al. [31]. There is also a reduction in measured static pressure on both vanes (by up to 10%) with nonuniform inlet conditions at the $x/C_{ax}=0.72$ tapping. It is not understood whether this is due to a real effect or due to measurement error.

At 50% span, both the measured and predicted cooled vane loading distributions show no significant change with the introduction of swirl. This is consistent with the small mid-span yaw angles (less than ± 5 deg) at turbine inlet at the positions of both vane LEs—see Fig. 2(f). For both inlet conditions, the cooled vane measurements are in excellent agreement with the predictions. For the uncooled vanes, however, the measured mid-span PS static pressures with swirl are consistently lower than on the cooled vanes. Furthermore, the measured static pressure is 3.9% lower on vane S1 (which is aligned with a swirler) than on vane S2. As discussed by Adams et al. [34] during commissioning of the combustor simulator, these measurements seem to be consistent with the presence of the swirler loss core. Figure 4 shows total pressure isosurfaces at 99.8% of \bar{p}_{01} , which illustrate the migration of the swirler loss core through the vane. The majority of the loss core passes along

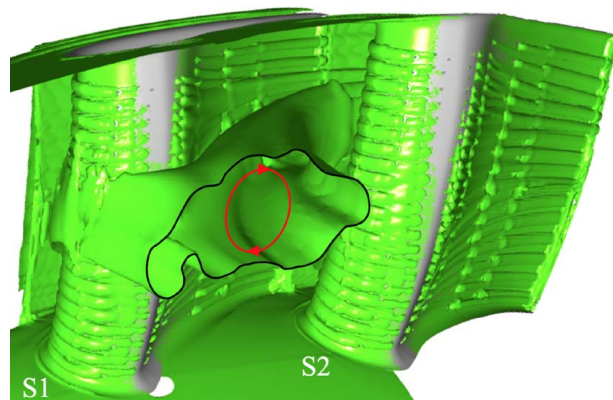


Fig. 4 Predicted total pressure isosurface at 99.8% of \bar{p}_{01} , with nonuniform inlet conditions, illustrating swirler loss core migration through the HP vane. The black line indicates the intersection of the isosurface with the vane inlet plane; the interior of the loss core is visible in the region bounded by this line. Arrows indicate (schematically) the orientation of the swirl vortex.

the PS (rather than the SS) of vane S1, which is consistent with the uncooled-vane measurements and also measurements presented in Refs. [26,29]. (It is noteworthy that the direction of the loss core migration is consistent with the net swirl around the annulus imparted by the individual swirler cores.) Uncooled CFD predictions did not show the same effect [34], which would appear to suggest that the total pressure deficit of the loss core was greater in the experiment than in the CFD BC. The p_{01} BC imposed in the CFD model (measured in a separate test facility at lower Re) has maximum variation of only $\pm 0.35\%$ —see Fig. 2(a)—which is an order of magnitude smaller than the static pressure change measured on vane S1 with swirl. Thus, while evidence points toward the presence of a significant loss core, the magnitude of the measured change in vane surface pressure is surprising. It is therefore not fully understood whether the reduced vane surface pressure in the region of the loss core is the result of a real effect. Possible explanations for the discrepancy include: a measurement error affecting only the uncooled mid-span PSappings (while all reasonable checks have been performed, the fact that only the measurements on uncooled vanes, and not cooled vanes, are affected points to the possibility of experimental error); the change in Re between atmospheric and OTRF test conditions causing an unexpected (i.e., caused by Re sensitivity) change in swirler loss. The difference being caused by Re-sensitive effect would seem unlikely (separated flows away from surfaces) but cannot not ruled out: OTRF studies of previous swirl simulators [17]—as well as URANS simulations of the present swirl simulator [34]—have indicated that the separated mixing flow downstream of the swirler is *not* Re-dependent (so far as loss is concerned).

At 90% span, the predicted static pressures on the early PS ($x/C_{ax} < 0.5$) of both cooled vanes are increased (by up to 2.5%) with swirl, while little change is predicted elsewhere. This causes a reduction in loading on the forward part of the vane and can be attributed to negative incidence near the casing, which is consistent with the positive yaw angles at turbine inlet at 90% span—see Fig. 2(f)—at the positions of the vane LEs. For both the cooled and uncooled vanes, the measurements show a static pressure increase (of up to 2.6%) on the early SS of vane S2 only. This is attributed to the greater incidence angle at the LE of vane S2 (+20.5 deg) compared with vane S1 (+17.1 deg)—see Fig. 2(f)—despite vane S2 being misaligned with the swirler.

In summary, the measured film-cooled HP vane surface pressure distributions are in reasonable agreement with the URANS predictions at 10% and 90% span, reflecting the expected changes due to positive and negative incidence, respectively. The measurements

and predictions at mid-span are in less good agreement and are difficult to reconcile. There is also poor agreement near the TE on the SS, in particular at 10% span, which is expected to be primarily due to a difference in geometry, rather than an error in the inlet BC.

The measured effects of a swirling inlet profile on the HP vane loading distributions are consistent with previous studies. In particular, Refs. [17,18] also reported increases/decreases in measured loading at 10%/90% span due to greater positive/negative incidence near the hub/casing, respectively, with swirl. However, the magnitude of the effects was greater in the referenced studies due to the higher strength of the swirl profile (peak yaw and pitch angles were greater than ± 40 deg, compared with approximately ± 30 deg in the present study).

High-Pressure Vane Surface Flow. Figure 5 shows predicted surface streamlines on uncooled HP vanes with uniform and nonuniform inlet conditions. Predictions are shown for uncooled rather than film-cooled vanes because the latter were severely distorted by the presence of the cooling sources.

With uniform inlet conditions, the streamline patterns are virtually identical for both vanes. The stagnation lines form relatively straight lines from hub to casing along the LE. Elsewhere on the PS and SS, the streamlines are largely parallel to the endwalls, except for relatively confined regions near the hub and casing, where endwall secondary flows are influential (in particular on the SS).

With nonuniform inlet conditions, the LE stagnation lines are deformed into S shapes on both vanes as a result of the altered incidence angles with swirl. Although only one vane has its LE aligned with the swirler, the degree of deformation is similar for both vanes. This observation is consistent with the inlet swirl profile: the vortex is not particularly localized but rather resembles a circumferential shear flow that should be expected to have a comparable effect on both vanes. There are, however, some differences: in contrast to the uniform inlet results, the PS streamline patterns with swirl are different for each vane. On the PS of vane S1, there is significant convergence of streamlines toward approximately 80% span, matched by divergence of streamlines arriving at the TE below mid-span. The streamline pattern on the PS of vane S2 is similar, but with streamline convergence toward approximately mid-span and with reduced severity, as the vane is not aligned with a swirler vortex. On the SS of both vanes, there is slightly increased

downwash with swirl, causing coolant to accumulate/dissipate below/above mid-span, respectively. The coolant, although not modeled in this particular simulation, is known to follow the mainstream flow on the SS.

Figure 6 shows predicted isosurfaces of total temperature effectiveness, defined as

$$\varepsilon = \frac{T_0 - T_{0c}}{T_{0h} - T_{0c}} \quad (1)$$

where T_0 is the local total temperature, T_{0h} is the hot stream total temperature exiting the swirler, and T_{0c} is the coolant total temperature (same for combustor simulator cold stream and HP vane film coolant). Isosurfaces are shown at $\varepsilon = 0.25$ for uniform and nonuniform inlet conditions in order to highlight the changes in film coolant and surface flow patterns. Note that the ε isosurfaces do not represent coolant concentration isosurfaces and are influenced—to a degree—by the inlet total temperature profile.

With uniform inlet conditions, coolant at some locations near the LE is injected into a nearly stagnant flow, appears to lift off from the vane surface (some coolant jets are ejected away from the surface and into the mainstream flow), and subsequently mixes out. At several locations, coolant from the leading PS row is swept toward the SS. This effect is typically undesirable for vane film-cooling systems and is due to the close proximity of the affected cooling holes to the LE stagnation line. As observed in Fig. 5(a), the stagnation line is approximately straight and therefore does not fit comfortably within the S-shaped gap between the leading rows of film-cooling holes, which was designed for robustness to inlet swirl and hence S-shaped LE stagnation lines. Elsewhere on the PS, coolant tends to follow the streamlines shown in Fig. 5(a).

With nonuniform inlet conditions, there appears to be little or no coolant liftoff near the LE, whereas with uniform inlet conditions some coolant jets were ejected away from the vane surface and into the mainstream flow, with nonuniform inlet conditions the coolant is instead quickly swept along the intended vane surfaces. This improvement in local coolant flow results from deformation of the stagnation lines into S shapes, which now fit more comfortably within the gap between the leading film-cooling rows. Elsewhere on the vanes—including the SS (not shown)—coolant follows the streamlines shown in Fig. 5(b).

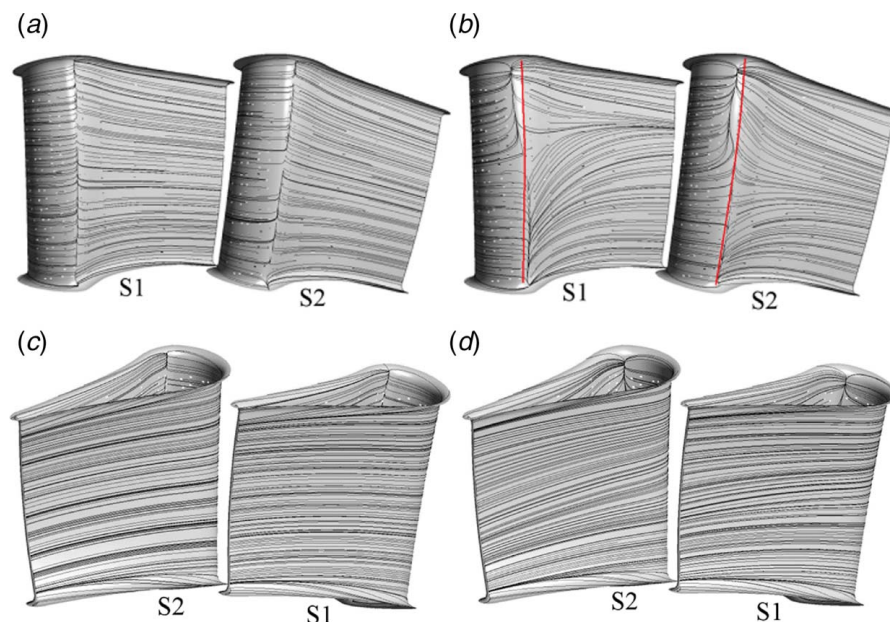


Fig. 5 Predicted surface streamlines on uncooled HP vanes: (a) uniform inlet (PS), (b) nonuniform inlet (PS), (c) uniform inlet (SS), and (d) nonuniform inlet (SS)

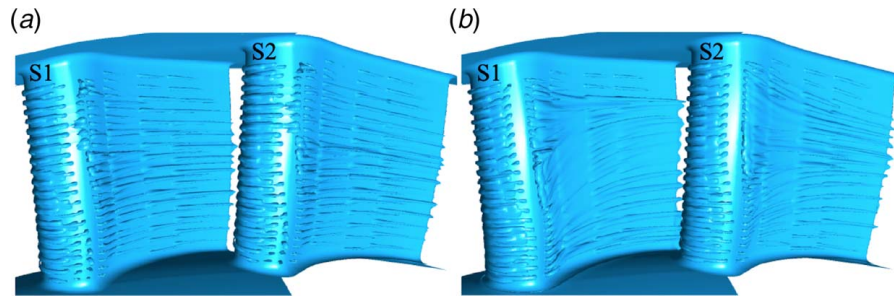


Fig. 6 Predicted isosurfaces at $\varepsilon = 0.25$, illustrating HP vane LE and PS film-coolant migration and surface flow patterns: (a) uniform inlet and (b) nonuniform inlet

High-Pressure Vane Total Pressure Loss. Increased/decreased HP vane loading causes increased/decreased flow velocities near the vane surfaces and thus increases/decreases BL loss, respectively. Additionally, changes to the vane surface flow patterns can be expected to affect loss by redistributing the coolant and BL fluid. Figure 7 compares URANS predictions of nondimensional total pressure loss coefficient distribution at HP vane exit ($x/C_{ax} = 1.32$) with uniform and nonuniform inlet conditions. The nondimensional total pressure loss coefficient is defined as

$$C_{p_0} = \frac{\bar{p}_{01} - p_{02}}{\bar{p}_{01} - \bar{p}_2} \quad (2)$$

where p_{02} is the local total pressure at vane exit, \bar{p}_{01} is the mass-averaged total pressure at turbine inlet, and \bar{p}_2 is the area-averaged static pressure at vane exit. The color-tone range (saturated at upper limit) has been chosen to best show differences between the fields.

With uniform inlet conditions, prominent loss cores are observed near the hub endwall as a result of the hub secondary flow vortices, which collect high-loss BL fluid from the hub endwall. Additional

high-loss regions are observed near the hub and casing; the thickness of these regions increase from PS to SS due to the endwall crossflows. Virtually identical vane wakes are observed, each exhibiting a radial nonuniformity due to the film-cooling sources at discrete points on the upstream vane surfaces.

The introduction of swirl is shown to significantly alter the shape of the vane wakes. This is most clearly observed for vane S1, where the wake is overturned above mid-span due to the negative incidence angles at vane inlet. For both vanes, losses in the wake region appear slightly reduced above mid-span and slightly increased below mid-span. The flow convergence observed at approximately 80% span on the PS of vane S1—see Fig. 6(b)—can be seen to result in greater loss at this span location in the wake of vane S1 than in the wake of vane S2. Furthermore, the loss cores associated with the hub endwall vortices appear enlarged with swirl. The secondary vorticity that develops due to turning of the hub BL at vane inlet is known to increase with the increase in the pitchwise gradient in streamwise velocity (increasing from PS to SS) that arises due to positive local incidence [37]. The enlargements in the loss cores associated with the hub secondary flow vortices observed Fig. 7 are likely due to this effect.

Figure 8 shows the predicted radial profiles of C_{p_0} at vane exit obtained by circumferentially mass-averaging the 2D distributions shown in Fig. 7. The greatest changes in loss are observed below 3% span and above 97% span, where loss is increased (by up to 7.0% of exit dynamic head) with nonuniform inlet conditions. These increases likely result from additional endwall crossflow causing collection of BL fluid in certain regions and therefore greater shear in other regions (where the BL has been thinned). There is also a slight increase in loss between approximately 20% and 40% span and a slight reduction in loss between 80% and 95% span. These changes are directionally consistent with the expected changes in loss due to increased/decreased vane loading below/above mid-span, respectively (see Fig. 3). However, the

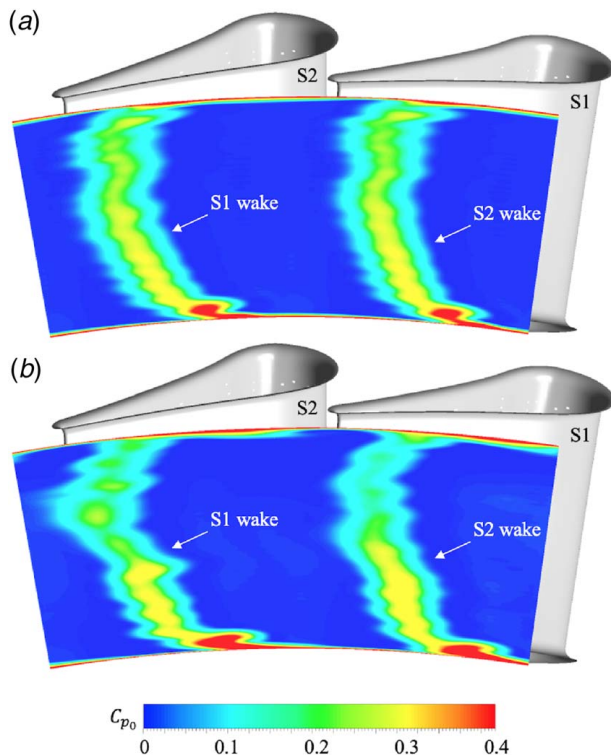


Fig. 7 Predicted total pressure loss coefficient distributions at HP vane exit with (a) uniform and (b) nonuniform inlet conditions

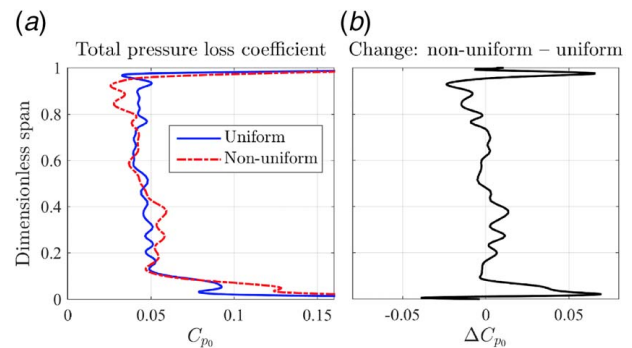


Fig. 8 Time-averaged predicted radial profiles of total pressure loss coefficient at HP vane exit: (a) with uniform and nonuniform inlet conditions and (b) difference with nonuniform inlet conditions

redistribution of film coolant due to swirl can also be expected to influence the loss distribution. It is observed in Fig. 6(b) that on the PS there is coolant accumulation at some span locations (near 80% span on vane S1 and near 60% on vane S2) and generally dissipation elsewhere; there is an overall accumulation above mid-span. Meanwhile, it is observed in Fig. 5(d) that on the SS there is slight downwash across most of the span (by about 5% of the span) and thus an overall accumulation below mid-span. Besides changes in coolant migration, the loss distributions are also affected by changes in the mainstream Mach number distribution: loss associated with SS coolant injection can be expected to increase with local mainstream Mach number at the cooling hole (source term) locations [38]. Since SS Mach numbers are increased/decreased below/above mid-span, respectively, this effect likely contributes to the increased/decreased loss above/below mid-span in Fig. 8.

The predicted mass-averaged total pressure loss coefficients are 5.65% and 5.70% for uniform and nonuniform inlet conditions, respectively. The change in loss coefficient is small, indicating that the loss increases/decreases below/above mid-span, respectively, approximately balance out. It is noteworthy that the combined circulation (around the machine axis) of the inlet swirl vortices is in the same direction as that of the vanes. This should be expected to result in net off-loading of the vanes and hence should be expected to contribute to loss reduction. That the predicted loss in fact increased with swirl suggests that this net off-loading effect is outweighed by the increases in loss outlined above.

In contrast to our results, URANS simulations reported by Beard et al. [20] predicted a significant increase in HP vane loss with swirl: the mixed-out total pressure loss coefficient increased by 11.5%. The increase in loss was significantly greater than reported in the present study for at least two reasons. First, the swirl profile was much more aggressive (peak swirl angles were greater than ± 40 deg compared with approximately ± 30 deg in the present study). Second, the vane had been designed for uniform inlet

conditions, whereas the vane in the present study was designed for robustness to inlet swirl [31].

Inlet Temperature Profile Convection Through High-Pressure Vane.

Figure 9 shows predicted total temperature effectiveness contours, calculated using Eq. (1), at HP vane exit with uniform and nonuniform inlet conditions. With uniform inlet conditions, the effectiveness distribution is dominated by film-cooled vane wakes. Thermal BLs are observed near the hub and casing, where heat has been lost to the isothermal endwalls (at 290 K).

With nonuniform inlet conditions, a significant total temperature nonuniformity has persisted through the passage. However, the nonuniformity has been distorted by the swirling mainstream flow, the vane secondary flows, and—to a degree—mixing with the hot stream. The film-cooled vane wakes also appear distorted by the swirl. In particular, evidence of significant coolant redistribution is observed in the wake of vane S1, with coolant accumulation (lower temperatures) at approximately 80% span matched by coolant dissipation (higher temperatures) above and below. This spanwise redistribution of coolant is consistent with the observations described for Fig. 6(b).

Figure 10(a) shows the predicted radial profiles of total temperature at HP vane inlet, T_{01} , and exit, T_{02} , with uniform and nonuniform inlet conditions. With uniform inlet conditions, the reduction in temperature between inlet and outlet of the vane due to coolant injection is fairly uniform across the span. With nonuniform inlet conditions, there are similar levels of temperature reduction near mid-span; however, the temperature reduction is nonuniform across the span as a result of coolant redistribution. In particular, there is virtually no temperature reduction below 15% span, indicating that radial redistribution/mixing of hot gas toward the hub offsets the local temperature reduction due to coolant injection.

Figure 10(b) shows the same profiles normalized by the local mass-mean values at each station: T_{01}/\bar{T}_{01} at vane inlet and T_{02}/\bar{T}_{02} at vane exit. These profiles highlight redistribution and mixing with the attenuation (offset) due to coolant injection effectively removed. With uniform inlet conditions, the total temperature profile at vane exit remains approximately uniform, indicating no significant radial redistribution of the film coolant, as is consistent with Figs. 6(a) and 6(c). The mass-mean total temperature attenuation across the vane is 2.92%, caused primarily by film coolant injection and secondarily by heat transfer to the endwalls. With nonuniform inlet conditions, the total temperature is reduced between approximately 25% and 80% span and increased at other span locations. This is consistent with a radially mixing temperature field convecting through the vane passage. A relatively pronounced local reduction in total temperature is observed close to 80% span as a result of film coolant accumulation on the PS of vane S1—see Fig. 6(a). The mass-mean total temperature reduction with non-uniform inlet conditions is 2.45%, which is smaller than with

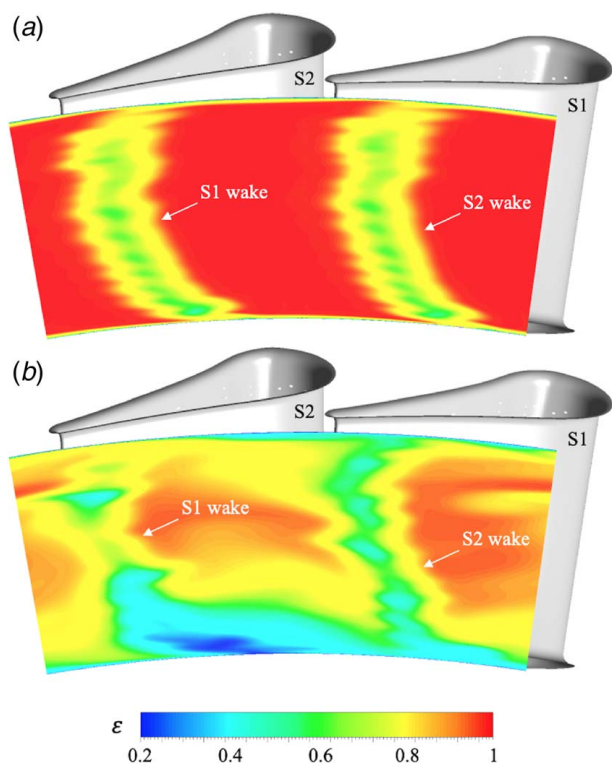


Fig. 9 Time-averaged predicted total temperature effectiveness distributions at HP vane exit with (a) uniform and (b) nonuniform inlet conditions

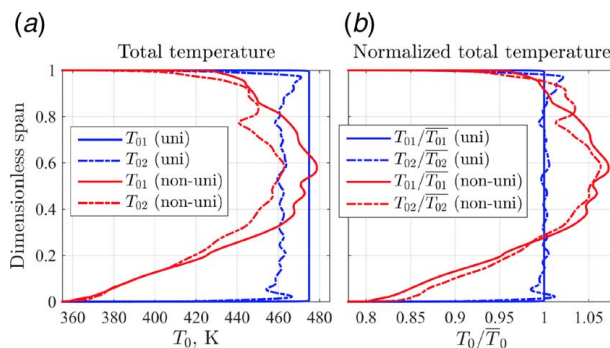


Fig. 10 Time-averaged predicted radial profiles of total temperature at HP vane inlet and exit: (a) in Kelvin and (b) normalized by their mass-mean values at each location

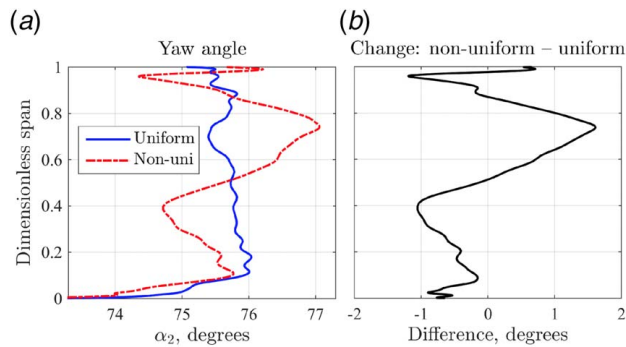


Fig. 11 Time-averaged predicted radial profiles of absolute yaw angle at HP vane exit: (a) with uniform and nonuniform inlet conditions and (b) difference with nonuniform inlet conditions

uniform inlet conditions (2.92%) likely due to reduced heat transfer caused by lower driving temperatures near the endwalls.

Radial Profiles at High-Pressure Vane Exit. Figure 11 shows predicted radial profiles of absolute yaw angle, α_2 , at HP vane exit with uniform and nonuniform inlet conditions and their difference (nonuniform minus uniform). With nonuniform inlet conditions, there is little residual swirl at vane exit (less than ± 1.5 deg) compared with that at inlet as a result of the strong flow acceleration in the vane. The small degree of residual swirl that does persist will contribute to positive/negative rotor incidence angles above/below mid-span, respectively.

Figure 12 shows predicted radial profiles of vane exit relative yaw angle, $\alpha_{2,rel}$. With uniform inlet conditions, the $\alpha_{2,rel}$ profile decreases from hub to casing as a result of the increasing rotor blade speed, U , with radius. With nonuniform inlet conditions, the changes in $\alpha_{2,rel}$ are significantly greater than the changes in α_2 . Increases of up to 2.4 deg are observed between 50% and 85% span, while reductions are observed across the remaining span. The largest reductions (of up to 12.7 deg) are observed near the endwalls. The changes in $\alpha_{2,rel}$ are influenced not only by residual swirl at vane exit but also (and to a greater degree) by the total temperature nonuniformity. For regions of hot gas near mid-span, $\alpha_{2,rel}$ should be increased, while for regions of cold gas near the endwalls, $\alpha_{2,rel}$ should be reduced. However, because the total temperatures near mid-span were not significantly increased with nonuniform inlet conditions—see Fig. 2(d)—the slight $\alpha_{2,rel}$ increases between 50–85% span are predominantly due to residual swirl.

Figure 13 shows predicted radial profiles of relative total pressure, $p_{02,rel}$, with uniform and nonuniform inlet conditions. With nonuniform inlet conditions, the $p_{02,rel}$ profile is changed

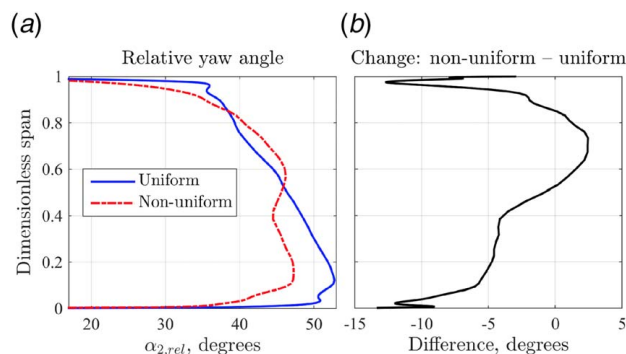


Fig. 12 Time-averaged predicted radial profiles of relative yaw angle at rotor inlet: (a) with uniform and nonuniform inlet conditions and (b) difference with nonuniform inlet conditions

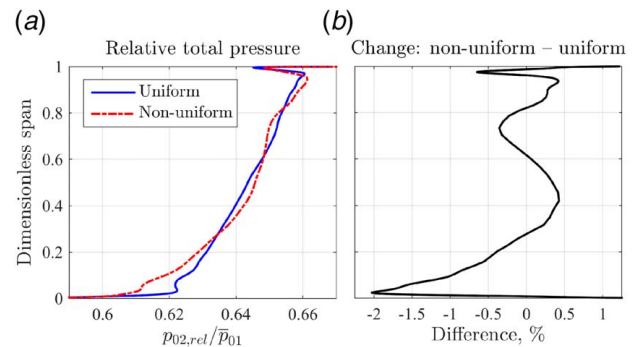


Fig. 13 Time-averaged predicted radial profiles of relative total pressure at rotor inlet: (a) with uniform and nonuniform inlet conditions and (b) percentage difference with nonuniform inlet conditions

significantly, with variations between -2% and $+0.5\%$. As discussed later, the increased gradients in the $p_{02,rel}$ profile can be expected to increase secondary vorticity in the rotor [2].

Figure 14 shows predicted radial profiles of relative total temperature, $T_{02,rel}$, with uniform and nonuniform inlet conditions. Data are plotted dimensionally (in units of Kelvin) rather than non-dimensionally because \bar{T}_{01} is different for the two cases, as discussed previously. With uniform inlet conditions, the $T_{02,rel}$ profile is relatively uniform, with spanwise variation of less than 20 K (4.2% of \bar{T}_{01}) outside of the thermal BLs. With nonuniform inlet conditions, the $T_{02,rel}$ profile is reduced (by up to 19%) at all span locations except near 50% span, where there is no change. This trend is consistent with the T_{01} profile shown in Fig. 2(d). The significant $T_{02,rel}$ nonuniformity would likely present challenges for rotor cooling systems optimized for uniform inlet conditions to the rotor or indeed the HP stage.

Rotor Aerodynamics

Rotor Blade Loading Distributions. Figure 15 shows predicted rotor blade loading distributions at 10%, 50%, and 90% span with uniform and nonuniform inlet conditions. Static pressure data have been normalized by the predicted mass-mean total pressure at rotor inlet, $\bar{p}_{02,rel}$.

At 10% span, static pressure is significantly increased (by up to 6.7%) on the early SS ($0 < x/C_{ax} < 0.45$) and slightly reduced (by up to 2.5%) along the entire PS. These changes indicate a reduction in loading on the forward part of the blade at 10% span. The peak static pressure, achieved where the LE stagnation line intercepts 10% span on the early PS, is reduced by 1.5%, which is consistent

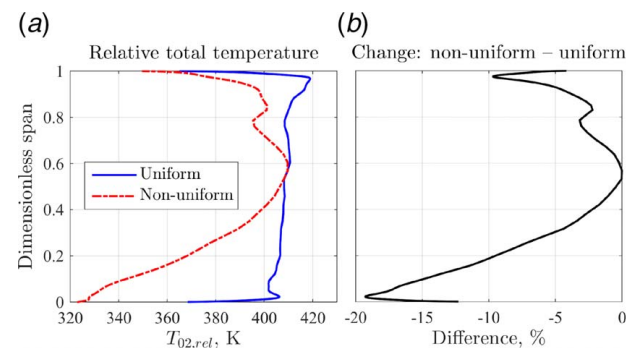


Fig. 14 Time-averaged predicted radial profiles of relative total temperature at rotor inlet: (a) with uniform and nonuniform inlet conditions and (b) percentage difference with nonuniform inlet conditions

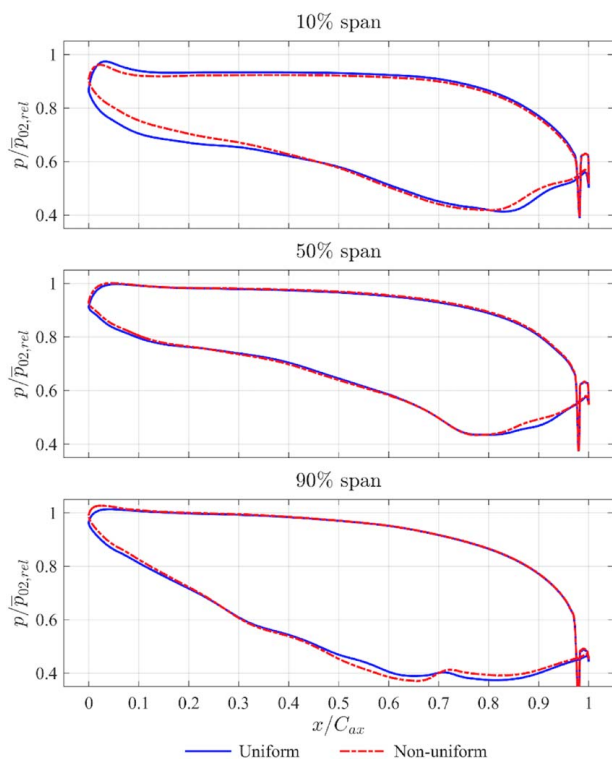


Fig. 15 Time-averaged predicted rotor blade loading distributions at 10%, 50%, and 90% span with uniform and nonuniform inlet conditions. Static pressure results have been normalized by $p_{02,rel}$.

with the similar reduction in $p_{02,rel}$ predicted at 10% span—see Fig. 13. Furthermore, close inspection shows that at 10% span, the stagnation line migrates a small distance (approximately 1% of C_{ax}) along the PS toward the LE, which is consistent with the predicted reduction in $\alpha_{2,rel}$ at 10% span—see Fig. 12. On the late SS ($0.8 < x/C_{ax} < 1$), the static pressure is increased by up to 7.2%; this contributes to reduced loading on the aft part of the blade at 10% span and is likely associated with altered secondary flow structure near the hub—see Fig. 16 (discussed later).

At 50% span, there is relatively little change to the blade loading distribution with nonuniform inlet conditions. Close inspection shows that on the early PS and SS ($0 < x/C_{ax} < 0.1$), static pressure is slightly increased (by up to 1.7%), which is consistent with the small predicted increase in $p_{02,rel}$ at mid-span—see Fig. 13. On the late SS ($0.8 < x/C_{ax} < 1$), a similar increase in static pressure (of up to 5.1%) is observed to that at 10% span.

At 90% span, static pressures on both the early PS and SS ($0 < x/C_{ax} < 0.1$) are increased by up to 2.5% with nonuniform inlet conditions, which is consistent with the small $p_{02,rel}$ increase predicted at 90% span—see Fig. 13. Further downstream on the SS, static pressure is reduced between 45–70% C_{ax} and increased between 70% and 100% C_{ax} (in both cases by up to 6.0%), likely due to altered tip leakage and secondary flow structures near the casing—see Fig. 16 (discussed later).

Rotor Surface Streamlines. Figure 16 shows time-averaged predicted streamlines on the rotor blade surfaces with uniform and nonuniform inlet conditions. On the SS, the region of the blade surface dominated by the lower passage vortex is larger with nonuniform inlet conditions than with uniform inlet conditions: at the TE, the affected region spans from 0% to 27% span with nonuniform inlet conditions, but only from 0 to 20% span with uniform inlet conditions. Near the blade tip, the regions of flow affected by the tip leakage and upper passage vortices are

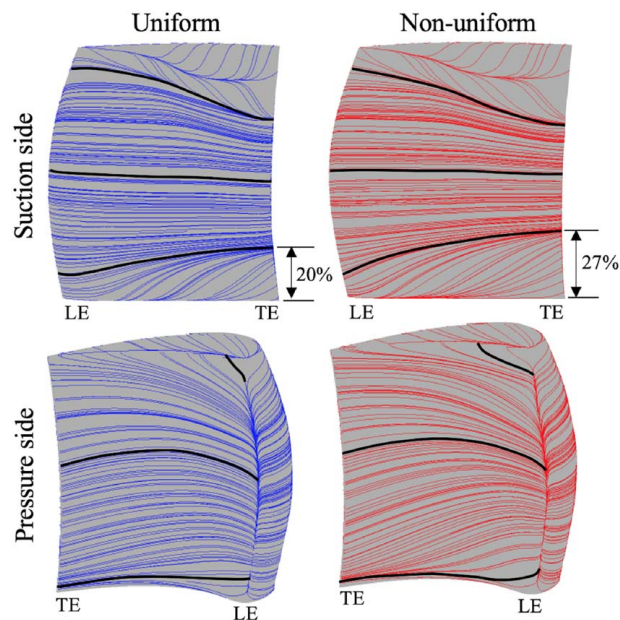


Fig. 16 Time-averaged predicted rotor blade surface streamlines with uniform and nonuniform inlet conditions. Streamlines seeded from the LE at 10%, 50%, and 90% span are highlighted.

relatively unaffected by the change in inlet conditions. There is, however, a small (almost imperceptible) increase in size of the upper passage vortex and decrease in size of the tip leakage vortex with nonuniform inlet conditions.

On the PS, streamlines below mid-span show stronger downwash with nonuniform inlet conditions than with uniform inlet conditions. This is consistent with an increase in strength of the lower passage vortex. Near the blade tip (above approximately 80% span), there is reduced upwash (streamlines are more axially aligned) with nonuniform inlet conditions. This likely results from the reduction in incidence angle in this region—see Fig. 12—and can be expected to contribute to reduced tip leakage flow. As is discussed later, a reduction in tip leakage flow would be consistent with a reduction in tip leakage vortex size and attendant loss. The PS streamlines also show increased streamline divergence with nonuniform inlet conditions for flow arriving at the TE between approximately 15–50% span. This is consistent with the predicted local maximum in rotor-relative inlet total pressure at approximately 40% span—see Fig. 13. The PS streamline divergence is also consistent with the predicted radial spreading out of hot gas on the PS (discussed later).

Rotor-Exit Total Temperature Survey. The rotor-exit total temperature profile, T_{03} , is expected to be the rotor-inlet total temperature profile, T_{02} , modified by redistribution and mixing of hot/cold gas, work extraction, and heat transfer to blade surfaces and endwalls. Area-survey measurements of T_{03} at rotor exit ($x/C_{ax} = 1.85$) are shown in Figs. 17(a) and 17(b) for uniform and nonuniform inlet conditions, respectively. The corresponding time-averaged URANS predictions are shown in Figs. 17(c) and 17(d). Radial profiles obtained by circumferentially area-averaging the measured/predicted contour maps are shown in Fig. 18. The experimental data have been normalized by \bar{T}_{01} to correct for small run-to-run variations in the mass flowrates and total temperatures of the individual gas streams supplied from the combustor simulator; for consistency, the predicted results have been normalized the same way. To first order, this normalization should also valid for the difference in \bar{T}_{01} between uniform/nonuniform inlet testing (which, as discussed, was not exactly matched). For uniform inlet conditions, the measured data (which covered only a single HP vane

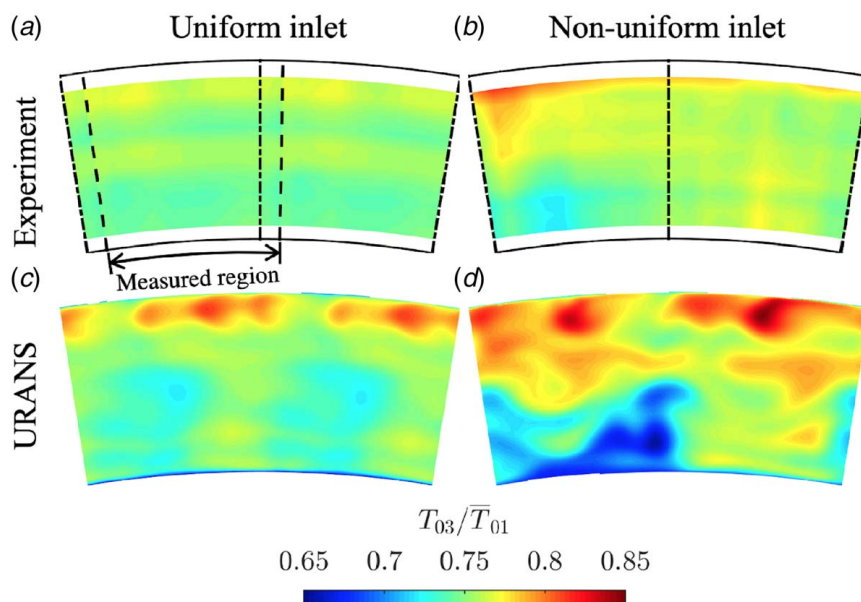


Fig. 17 Measured (a, b) and time-averaged predicted (c, d) total temperature distributions (normalized by \bar{T}_{01}) at the rotor-exit traverse plane with uniform (a, c) and nonuniform (b, d) inlet conditions, as viewed from downstream. Dot-dashed lines indicate circumferential position of HP vane LEs. Swirler is aligned with top-dead-center.

pitch) have been replicated to cover two HP vane pitches, i.e., a full combustor simulator pitch, to allow clearer comparison with the measurements with nonuniform inlet conditions (which covered two HP vane pitches or equivalently a single combustor simulator pitch).

With uniform inlet conditions, the measured T_{03} profile is dominated by a radial nonuniformity, with circumferential streaks of relatively hot gas between 40% and 60% span and above 80% span. The highest temperatures are measured above 80% span, likely due to lower work extraction in the blade tip region. Elsewhere, the temperature is relatively uniform: in particular, there is little evidence of cold HP vane wakes.

The URANS predictions also show circumferential streaks of hot gas with uniform inlet conditions. In particular, a circumferential streak of hot gas is predicted near the casing (above approximately 85% span), although the predicted temperatures in this region (up to 84.8% of \bar{T}_{01}) significantly exceed the measurements. In contrast to the measurements, pronounced HP vane wakes can be observed as relatively low-temperature regions.

With nonuniform inlet conditions, the measured T_{03} contours show more severe nonuniformity, both radially and circumferentially, than with uniform inlet conditions. For example, the ratio

of global maximum to mass-mean total temperature at rotor exit, $T_{03}^{max}/\bar{T}_{03}$, is 1.069, compared with 1.059 with uniform inlet conditions. The highest temperatures are again measured near the casing at the outer radial limit of the measured region. The predicted T_{03} contours show more severe nonuniformity than the measurements. There are, however, some shared general features, including peak temperatures near the casing and a fairly localized region of cold gas below mid-span.

Figure 18(b) highlights the differences between the measured and predicted radial T_{03} profiles. With the introduction of nonuniform inlet conditions, the measurements show an approximately uniform increase in T_{03} , indicating a reduction in specific work extraction of the rotor. In contrast, the predictions show a pronounced radial nonuniformity that increases from hub to casing, rather than an approximately constant increase in temperature. The discrepancy between measurement and prediction suggests a failure of the URANS model in accurately predicting the complex effects of the change in inlet conditions on the mixing, redistribution, and work extraction processes in the HP stage. In particular, it appears that the radial convection of the hot-streak (coolant) toward the casing (hub)—which might be expected to be dominant—is overpredicted.

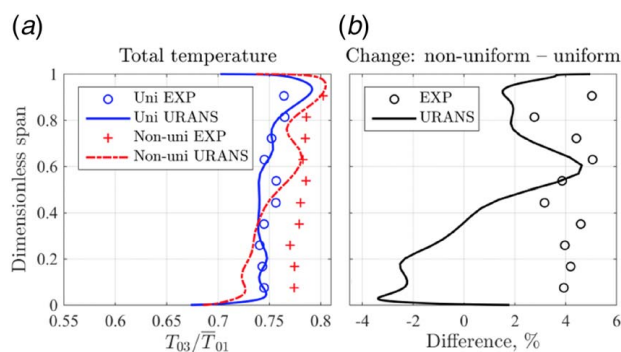


Fig. 18 Measured and time-averaged predicted radial profiles of total temperature (normalized by \bar{T}_{01}) at the rotor-exit traverse plane: (a) with uniform and nonuniform inlet conditions and (b) difference between uniform and nonuniform inlet conditions

Rotor-Relative Flow Field. To understand how the introduction of nonuniform inlet conditions affects the aerodynamics of the rotor, we now study the rotor-relative flow. We first examine the migration of hot and cold gas in the rotor and then examine the total pressure losses.

Migration of Hot and Cold Gas Within the Rotor. Figure 19 shows time-averaged predicted contours of relative total temperature at the rotor-exit traverse plane with uniform and nonuniform inlet conditions. Because these results are resolved in the rotating frame, the contours show features associated with the rotor blades rather than the HP vanes or the turbine inlet profile (which are effectively circumferentially mixed out in this frame by time-averaging). The corresponding radial profiles (circumferentially mass-averaged) are shown in Fig. 20; the rotor-inlet radial profiles shown in Fig. 14 are reproduced for reference. The profiles have

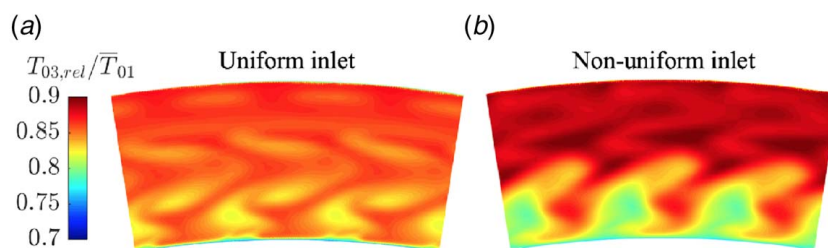


Fig. 19 Time-averaged predictions of relative total temperature (normalized by \bar{T}_{01}) at the rotor-exit traverse plane with (a) uniform and (b) nonuniform inlet conditions, as viewed from downstream. Results are shown over three rotor blade pitches.

been normalized by \bar{T}_{01} to allow comparison between the two turbine inlet conditions.

With uniform inlet conditions, the $T_{03,rel}$ contours are predominantly characterized by low-temperature features where cold gas has accumulated in the deformed rotor blade wakes and secondary flow vortices (in particular below mid-span). The corresponding circumferentially averaged profile shows relatively little radial variation and is slightly reduced (by up to 1.9%) with respect to the rotor-inlet profile across most of the passage height as a result of convective heat transfer to the rotor blade surfaces.

The mechanisms responsible for the $T_{03,rel}$ distribution with uniform inlet conditions can be explained with reference to Fig. 21, which shows time-averaged predicted $T_{0,rel}$ contours at six axial planes throughout the rotor ($0 < x/C_{ax} < 1.25$). At rotor inlet ($x/C_{ax}=0$), the time-averaged $T_{0,rel}$ profile is relatively uniform, with only slight radial variation increasing from hub to casing (this is consistent with the radial profile shown in Fig. 14). In this (rotor-relative) frame, the HP vanes move with respect to the stationary rotor, rendering the time-averaged flow almost perfectly uniform in the circumferential direction. As we will see, however, the time-instantaneous variations in temperature (which are not apparent in the inlet flow in this frame of reference) lead to flow segregation as we progress further through the rotor passage. At $x/C_{ax}=0.25$, regions of hot and cold gas can be seen near the PS and SS, respectively, as a result of preferential migration of hot mainstream gas toward the PS and cold gas (from the film-cooled HP vane wakes) toward the SS. As the flow progresses through the rotor passage, the degree of segregation (due to preferential migration) increases. By $x/C_{ax}=1$, significant amounts of cold gas have become entrained in the hub passage and tip leakage vortices. Between the rotor TE and the traverse plane ($1 < x/C_{ax} < 2$), the regions of segregated hot and cold gas partially mix out. At $x/C_{ax}=1.25$, entrainment of hot gas between the tip leakage and upper passage vortices can be observed; the enhanced mixing in this region (driven by the high secondary kinetic energy associated with the tip leakage vortex in particular) results in

the relatively uniform $T_{03,rel}$ distribution toward the casing, compared with that toward the hub, at the downstream traverse plane ($x/C_{ax}=2$)—see Fig. 19(a).

With nonuniform inlet conditions, the predicted $T_{03,rel}$ contours, shown in Fig. 19(b), differ significantly from those with uniform inlet conditions. In particular, there is greater radial nonuniformity, with increased segregation of hot/cold gas above/below mid-span. We see in the corresponding radial profiles, shown in Fig. 20, that the $T_{0,rel}$ nonuniformity at rotor exit is nevertheless substantially reduced compared with that at inlet, indicating that the non-uniform $T_{0,rel}$ profile at rotor inlet mixes out radially as it convects through the rotor.

The mechanism responsible for the $T_{03,rel}$ distribution with non-uniform inlet conditions can be explained with reference to the time-averaged predicted $T_{0,rel}$ contours shown at axial planes throughout the rotor in Fig. 22. At rotor inlet ($x/C_{ax}=0$), the time-averaged $T_{0,rel}$ profile is relatively uniform circumferentially but features a strong radial nonuniformity, with cold gas near the endwalls and hot gas near mid-span. This nonuniformity is consistent with the radial profile shown in Fig. 14. As the flow progresses through the rotor, two effects take place simultaneously. First, there is preferential migration of hot/cold gas toward the PS/SS, respectively, as was also observed with uniform inlet conditions. Evidence of this effect appears as early as $x/C_{ax}=0.25$ and becomes more pronounced with axial distance through the rotor. Second, hot gas near the PS migrates radially toward the endwalls, while cold gas near the hub and casing migrates along the endwalls toward the SS. This effect was first described by Butler et al. [2] and results from the classical secondary flow vorticity in the rotor

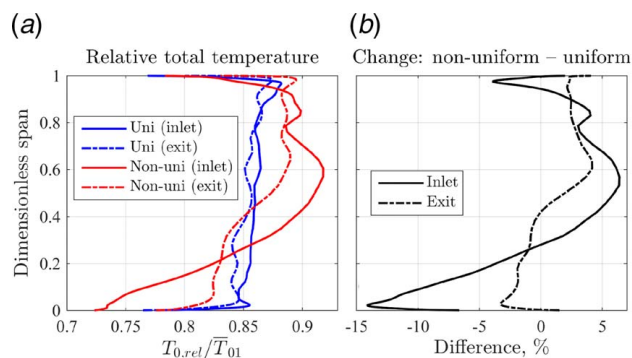


Fig. 20 Time-averaged predicted radial profiles of relative total temperature (normalized by \bar{T}_{01}) at rotor inlet and exit: (a) with uniform and nonuniform inlet conditions and (b) difference with nonuniform inlet conditions

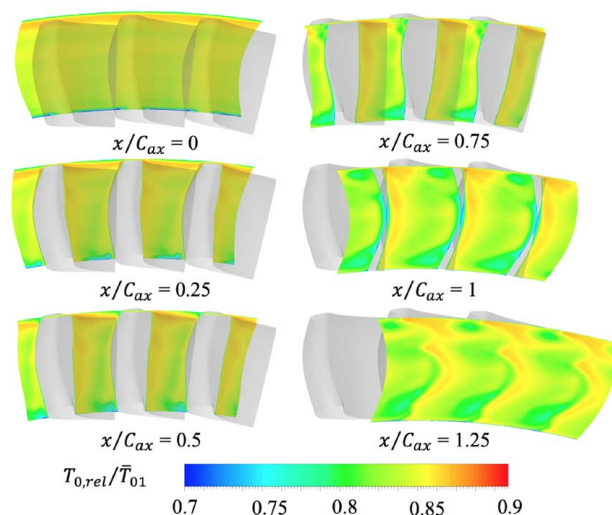


Fig. 21 Time-averaged predicted relative total temperature contours (normalized by \bar{T}_{01}) at axial planes throughout the rotor passage with uniform turbine inlet conditions. Viewing orientation is from downstream of the rotor blades.

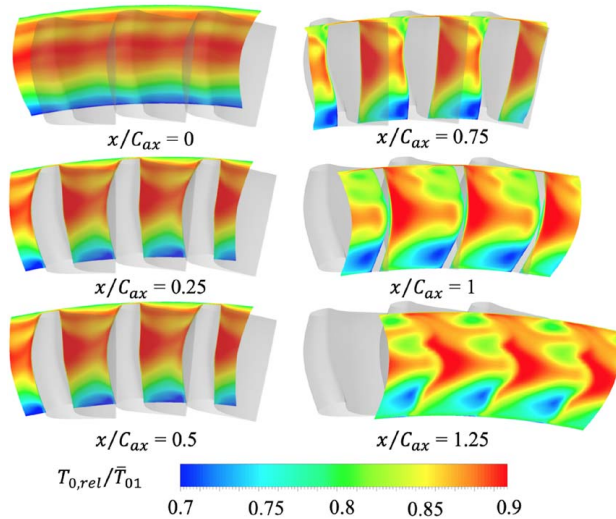


Fig. 22 Time-averaged predicted relative total temperature contours (normalized by T_{01}) at axial planes throughout the rotor passage with nonuniform turbine inlet conditions. Viewing orientation is from downstream of the rotor blades.

(which, as discussed, is likely augmented by the increased radial gradients in the rotor-relative inlet stagnation conditions).

At rotor exit ($x/C_{ax} = 1$), much of the cold gas has been entrained in the secondary flow vortex cores. The lowest temperatures are observed within the hub secondary flow vortices, due to the lower relative total temperatures near the hub at rotor inlet. Between the rotor TE and the traverse plane ($1 < x/C_{ax} < 2$), the $T_{0,rel}$ nonuniformity partially mixes out. Entrainment of hot gas between the counterrotating tip leakage and upper passage vortices is again clearly observed at $x/C_{ax} = 1.25$. The higher degree of mixing in this region gives rise to the relatively uniform $T_{03,rel}$ field observed above mid-span at the rotor-exit traverse plane ($x/C_{ax} = 2$), whereas regions of relatively unmixed cold gas are observed below mid-span—see Fig. 19(b).

Rotor-Relative Total Pressure Loss. Figure 23 shows time-averaged predicted contours of rotor-relative total pressure, $p_{03,rel}$, at the rotor-exit traverse plane with uniform and nonuniform inlet conditions. The corresponding radial profiles (circumferentially mass-averaged) are shown in Fig. 24; the rotor-inlet radial profiles shown in Fig. 13 are reproduced for reference. With both inlet conditions, the predicted $p_{03,rel}$ contours show clear high-loss regions corresponding to the blade wake and secondary flows. Most prominent are the tip leakage vortices, which are observed just below the casing.

With nonuniform inlet conditions, the size and relative total pressure deficit associated with the tip leakage vortices appear significantly reduced. The radial profiles indicate a 4.4% increase in circumferentially averaged $p_{03,rel}$ at 90% span (the approximate location of the vortex centers), which is large compared with the

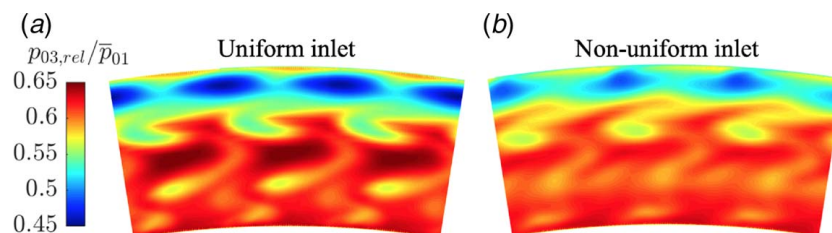


Fig. 23 Time-averaged predictions of relative total pressure (normalized by \bar{p}_{01}) at the rotor-exit traverse plane with (a) uniform and (b) nonuniform inlet conditions, as viewed from downstream. Data are shown over three rotor blade pitches.

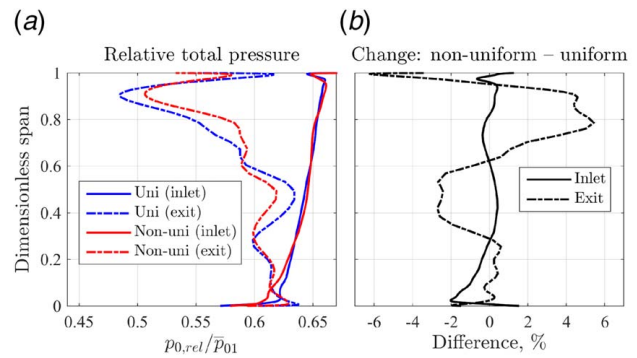


Fig. 24 Time-averaged predicted radial profiles of relative total pressure (normalized by \bar{p}_{01}) at rotor inlet and exit: (a) with uniform and nonuniform inlet conditions and (b) difference with nonuniform inlet conditions

changes in rotor-inlet $p_{02,rel}$ at the same span location, thus indicating a reduction in tip leakage loss. The predicted reduction in tip leakage loss is consistent with the changes in predicted streamline patterns shown in Fig. 16: PS streamlines near the blade tip were directed more axially (i.e., away from the tip gap) and on the SS, the footprint of the tip leakage vortex was slightly reduced in size.

The next most prominent loss cores are associated with the upper passage vortices, visible just below the tip leakage vortices, at approximately 60% span. With nonuniform inlet conditions, these loss cores appear smaller and more distinct from the tip leakage vortex loss cores and their associated $p_{03,rel}$ deficit is reduced. This is likely due to the smaller tip leakage vortex causing less radial mixing out; with less interaction between the two vortices, there should be less conversion of secondary kinetic energy to total pressure loss.

With uniform inlet conditions, there is a region near mid-span (40–60% span) between the blade wakes, where the influence due to secondary flows is small (low loss) and thus local $p_{0,rel}$ is high. Note that this is despite the small increase in $p_{02,rel}$ (by 0.4%) near mid-span with nonuniform inlet conditions—see Fig. 13. With nonuniform inlet conditions, the larger lower and upper passage vortices—see Fig. 16—cause greater loss in this region. The corresponding radial profile indicates a reduction in circumferentially averaged $p_{03,rel}$ by up to 2.7% near mid-span.

Below approximately 30% span, the $p_{03,rel}$ contours show evidence of the hub secondary flows. With nonuniform inlet conditions, the associated loss cores are more mixed out than with uniform inlet conditions, but the circumferentially averaged $p_{03,rel}$ profiles show only small changes of less than 0.5%. Given that $p_{02,rel}$ is reduced by up to 2% in this region with nonuniform inlet conditions (see Fig. 13), this suggests a reduction in loss near the hub. On one hand, loss near the hub could be expected to decrease due to the reduction in blade loading near the hub (see Fig. 15). On the other hand, loss could be expected to increase as a result of increased secondary vorticity. It is likely that these two effects compete, with the loss reduction mechanism dominating in this case.

Absolute Radial Profiles at Rotor Exit. Before examining the IP vane aerodynamics, we briefly discuss the time-averaged absolute flow at rotor exit. Figure 25 shows predicted radial profiles of circumferentially mass-averaged yaw angle, α_3 , Mach number, M_3 , total pressure, p_{03} , and static pressure, p_3 , at the rotor-exit traverse plane.

With nonuniform inlet conditions, Fig. 25(a) shows smaller peak positive and negative yaw angles (with respect to the mean) at approximately 80% and 90% span than with uniform inlet conditions. This is consistent with the reduction in strength of the tip leakage vortex (discussed previously), which dominates the flow in this region. Additionally, the local minimum in α_3 at approximately 90% span (due to under-turning associated with the tip leakage vortex) is radially displaced slightly toward the casing. This is consistent with the SS streamline patterns shown in Fig. 16, which suggested a reduction in size of the tip leakage vortex with nonuniform inlet conditions. The largest change in α_3 , however, is observed between approximately 30–60% span, where the absolute value of α_3 is reduced by up to 8.6 deg with nonuniform inlet conditions. This reduction, which corresponds to an increase in incidence angle near mid-span at inlet to the (co-turning) IP vane, is a result of increased secondary flow influence near mid-span—see associated total pressure deficit in Fig. 24—which causes under-turning of the flow and reduced $p_{03,rel}$ in this region. Note that while partial preservation of the hot-streak through the stage would result in hot gas near mid-span at exit, and therefore temperature-induced increase in absolute value of α_3 near mid-span, no such effect occurred because the mass-mean total temperature was lower with nonuniform inlet conditions than with uniform inlet conditions—see Fig. 2(d).

For both inlet conditions, the M_3 and p_{03} profiles shown in Figs. 25(c) and 25(d), respectively, bear close resemblance to one another. This is consistent with the relatively small changes (increase) in p_3 observed across the span—see Fig. 25(d). Between approximately 70–90% span, p_{03} increases (by up to 2.4%) due to the reduction in tip leakage loss. Below 30% span, p_{03} is reduced (by up to 2.1%) with nonuniform inlet conditions, as a result of increased secondary flow near the hub.

Intermediate-Pressure Vane Aerodynamics

Intermediate-Pressure Vane Loading Distributions.

Figure 26 shows measured and predicted IP vane loading distributions at 10%, 50%, and 90% span with uniform and nonuniform

inlet conditions. All measured data have been averaged over at least two good test runs. At 10% span, the measured and predicted IP vane loading distributions show little change with the introduction of nonuniform inlet conditions. The most pronounced change is observed on the early SS near the LE ($0 < x/C_{ax} < 0.1$), where the predictions show reduced static pressure (by up to 3.8%) and the limited measurements in this region (at $x/C_{ax} \approx 0.00$ and 0.11) show comparable reductions (of 2.9% and 2.4%, respectively). These results are consistent with the predicted increase in incidence angle (note: IP vane is co-turning) near the hub—see Fig. 25(a). Because the static pressure distribution on the PS is comparatively unchanged, loading on the forward part of the vane is slightly increased. Further downstream on the SS ($0.5 < x/C_{ax} < 0.8$), the measured static pressures are increased with nonuniform inlet conditions, while the predictions show no change. This could be due to a change in secondary flow near the hub, which is not captured by the CFD model (the complex nature of the secondary flows is discussed in a later section of this paper, “Intermediate-Pressure Vane Exit Survey”).

At mid-span, the predicted static pressure distributions near the LE ($0 < x/C_{ax} < 0.03$) indicate that for both inlet conditions, the stagnation line lies slightly toward the SS, rather than at $x/C_{ax} = 0$. (Note: with the results plotted against x/C_{ax} , the delineation between PS/SS is somewhat arbitrary, as it does not correspond to the actual stagnation point). With nonuniform inlet conditions, the predictions show increased loading between $0.03 < x/C_{ax} < 0.5$ due to increased/decreased static pressure on the PS/SS, respectively. The measured static pressures in this region are in directional agreement with the predictions on both the PS and SS, although the measured changes are smaller than the predicted changes. The increased loading in this region is consistent with the reduced α_3 near mid-span observed in Fig. 25(a), which results in increased incidence angle at the IP vane LE. Between approximately $0.35 < x/C_{ax} < 0.65$, the measurements show a reduction in static pressure on the SS with nonuniform inlet conditions, which is not observed in the prediction. This may be due to a difference in surface secondary flow structure induced by the change in inlet condition—the secondary flows are complex as will be shown in a later section of this paper, “Intermediate-Pressure Vane Exit Survey”. Elsewhere at mid-span, the measurements and predictions both show little change with the introduction of nonuniform inlet conditions and are in good agreement with each other.

At 90% span, the predicted peak static pressure (achieved at the LE) is reduced with the introduction nonuniform inlet conditions, despite the predicted increase in p_{03} at 90% span shown in

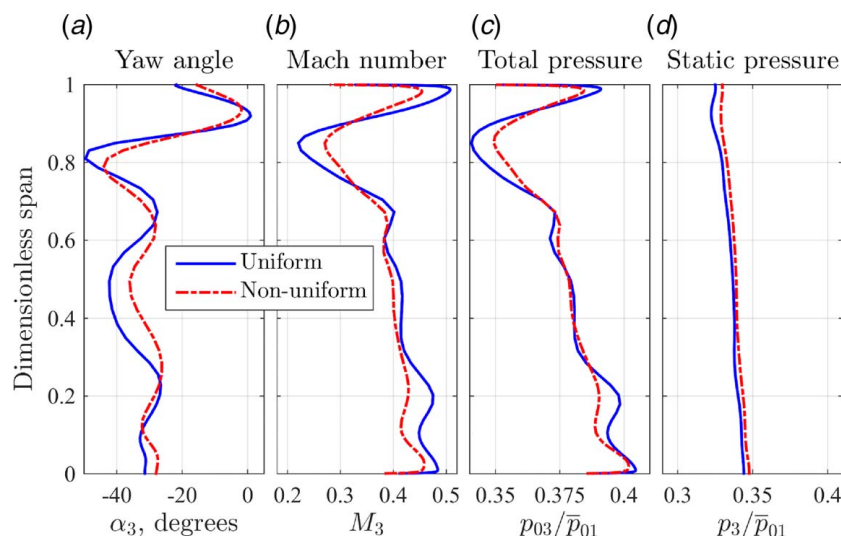


Fig. 25 Time-averaged predicted radial profiles at the rotor-exit traverse plane with uniform and nonuniform inlet conditions: (a) yaw angle, (b) Mach number, (c) total pressure, and (d) static pressure. Pressure results have been normalized by p_{01} .

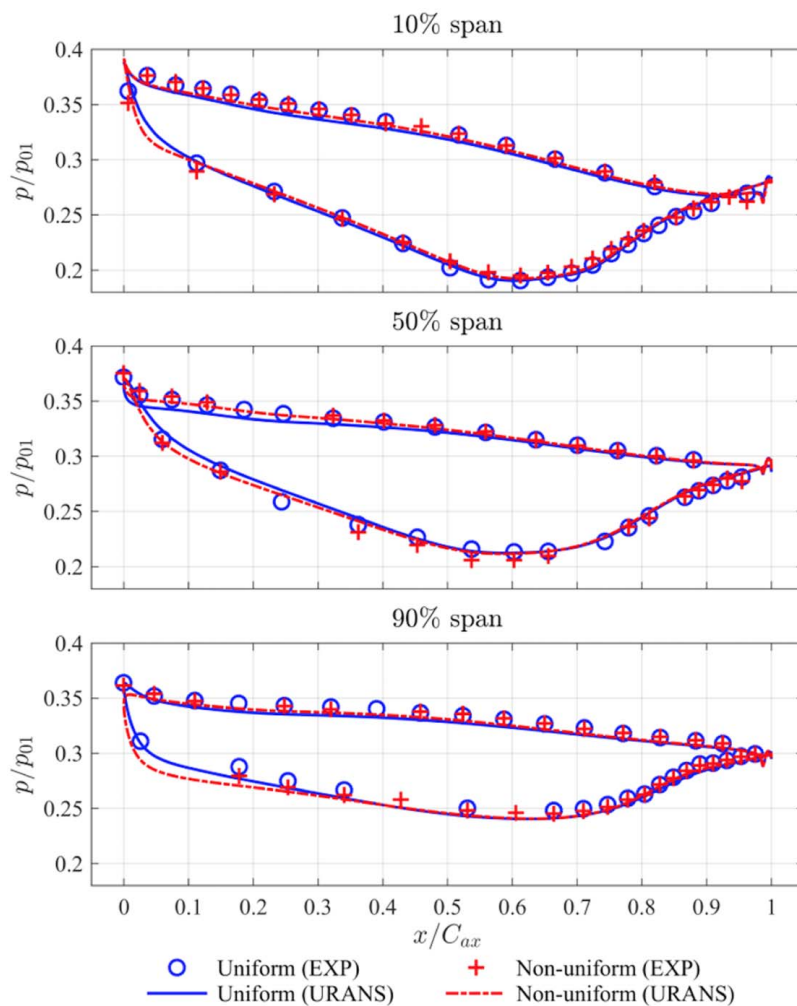


Fig. 26 Measured (markers) and time-averaged predicted (lines) IP vane loading distributions at 10%, 50%, and 90% span with uniform and nonuniform inlet conditions. Static pressure results have been normalized by \bar{p}_{01} .

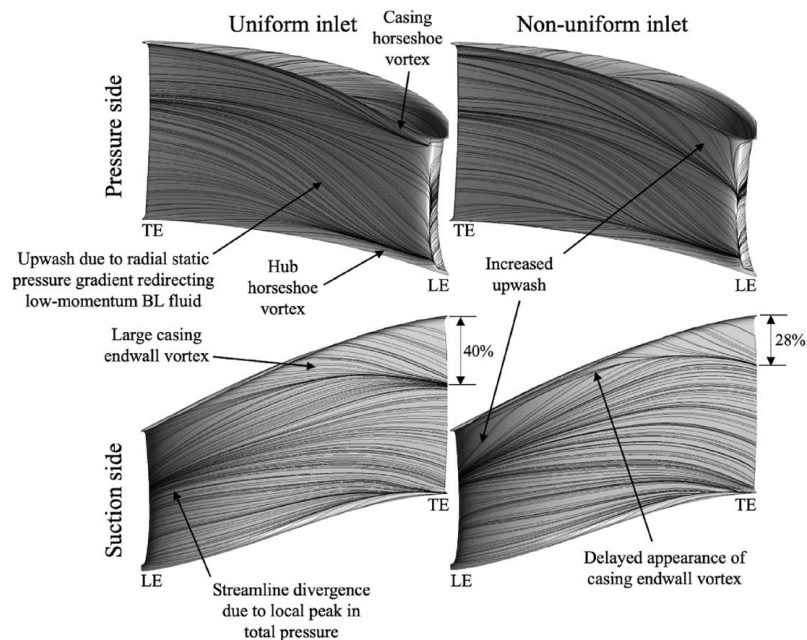


Fig. 27 Time-averaged predicted IP vane surface streamlines with uniform and nonuniform inlet conditions

Fig. 25(c). This is explained by the corresponding change in surface streamline patterns: Fig. 27 (discussed later) shows significantly increased radial migration toward the casing above approximately 60% span near the LE, which should be expected to result in static pressures below the total pressure in this region. There is comparatively little evidence of this effect in the measurements, however, which show virtually no change in peak static pressure at the LE.

Also at 90% span, the predictions show increased loading on the forward part of the vane ($0 < x/C_{ax} < 0.3$), caused predominantly by reduced static pressure on the SS. This is also suggested by the change in streamline patterns: Fig. 27 shows greater streamline divergence in this region with nonuniform inlet conditions than with uniform inlet conditions. The limited measurements on the early SS ($0 < x/C_{ax} < 0.3$) also indicate reduced static pressure, which is consistent with streamline divergence. Elsewhere at 90% span, the measurements and predictions show little difference due to the change in inlet conditions.

Intermediate-Pressure Vane Surface Streamlines. Figure 27 shows time-averaged predicted streamlines on the IP vane PS and SS surfaces with uniform and nonuniform inlet conditions. With uniform inlet conditions, the PS streamlines emanating from below mid-span at the LE show strong radial migration toward the casing, or upwash, caused by the radial static pressure gradient (associated with the duct curvature in the meridional plane) redirecting low-momentum BL fluid. Near the endwalls, there is evidence of secondary flows: horseshoe vortices form upstream of the LE and cause downwash/upwash near the hub/casing, respectively. Meanwhile, SS streamlines emanating from approximately 60% span at the LE diverge: this is likely associated with the local peak in total pressure at this span location—see Fig. 25(c). Near the casing, a large endwall vortex causes flow migration onto the SS: at the TE, the flow migration reaches 40% of the span measured from the casing. A significantly smaller endwall vortex is observed on the hub SS fillet.

The introduction of nonuniform inlet conditions causes significant changes to the predicted IP vane surface streamline patterns. At the LE, streamlines above approximately 70% span on both the PS and SS are directed radially toward the casing. This causes upwash along a significant portion of the near-casing PS (consistent with a counter-clockwise vortex viewed from upstream) and delays the appearance of the casing endwall vortex on the SS. As a result, flow migration onto the SS due to the casing endwall vortex reaches only 28% of the vane span at the TE (measured from the casing) compared with 40% with uniform inlet conditions. Below mid-span on both the PS and SS, changes to the streamline patterns due to nonuniform inlet conditions are comparatively small.

Figure 28 shows time-averaged predicted streamlines on the hub and casing endwalls with uniform and nonuniform inlet conditions. With nonuniform inlet conditions, the casing endwall vortex that forms near the PS is significantly larger than with uniform inlet conditions. This vortex enhances the endwall crossflow toward and onto the SS as was observed in Fig. 27. Meanwhile, a counterrotating endwall vortex forms adjacent to the early SS and delays flow migration from the casing endwall onto the SS.

Intermediate-Pressure Vane Exit Survey. Figure 29 presents measured and predicted area contours, at the IP vane exit traverse plane ($x/C_{ax} = 1.43$), of total temperature, T_{04} , static pressure, p_4 , Mach number, M_4 , total pressure, p_{04} , and yaw angle, α_4 . Results are shown for uniform and nonuniform inlet conditions. All measured data have been averaged over at least two good test runs. The traverse measurements (which cover approximately 1.25 IP vane pitches or equivalently 1.25 combustor simulator pitches) have been replicated to cover two IP vane pitches, which corresponds to two combustor simulator pitches. The measured region is indicated in the top-left subfigure. Radial profiles obtained by

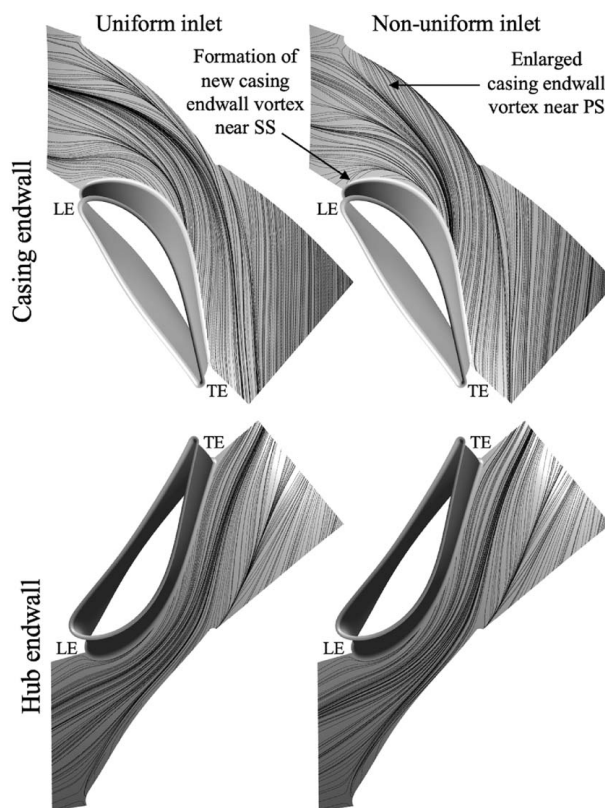


Fig. 28 Time-averaged predicted IP vane hub and casing endwall streamlines with uniform and nonuniform inlet conditions

circumferentially mass-averaging the measured and predicted area contours are shown in Fig. 30.

Figure 29(a) shows measured and predicted total temperature area contours at the IP vane exit traverse plane, T_{04} . There is generally good agreement between the measured and predicted contours, with both showing more pronounced nonuniformity (in both the radial and circumferential directions) with nonuniform inlet conditions. To quantify the degree of total temperature nonuniformity at IP vane exit—or indeed any station throughout the turbine—we define two global total temperature nonuniformity parameters (note that many alternative and equally valid metrics also exist). The first parameter

$$Q = \frac{T_0^{max} - \bar{T}_0}{\bar{T}_0} \quad (3)$$

describes the difference between the maximum and mass-mean total temperatures, emphasizing peaks rather than troughs in the field. The second parameter

$$Q' = \frac{\text{rms}(T_0 - \bar{T}_0)}{\bar{T}_0} \quad (4)$$

describes the root-mean-square (rms) variation about the mass-mean total temperature, giving a more holistic measure of nonuniformity. For both parameters, higher values indicate stronger nonuniformity.

It is noted that RANS/URANS simulations are known to typically underpredict mixing. Such an overprediction is evident in Fig. 29(a), where the predicted T_{04}/T_{01} distributions show greater nonuniformity than the experimentally measured distributions. As a result, predictions of Q and Q' are likely to be higher than would be achieved in experiments. Nevertheless, analysis of the general trends with and without nonuniform inlet conditions, and

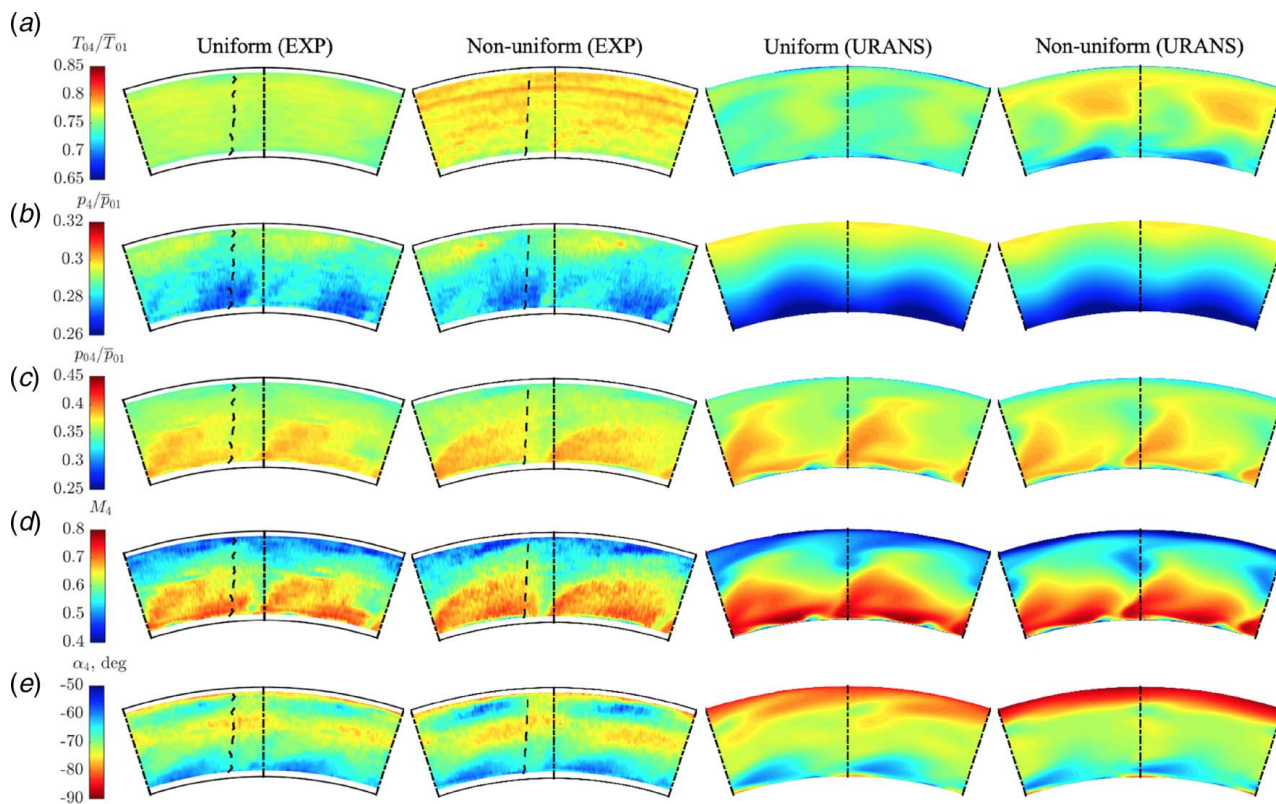


Fig. 29 Area-survey measurements and time-averaged URANS predictions at the IP vane exit traverse plane with uniform and nonuniform inlet conditions, as viewed from downstream: (a) total temperature, (b) static pressure, (c) total pressure, (d) Mach number, and (e) yaw angle. Dashed lines separate original and replicated measurements; dot-dashed lines indicate swirler pitch lines.

at different axial stations throughout the machine, should still be insightful even if the absolute magnitudes are overpredicted.

The bar chart shown in Fig. 31 presents predicted values of Q and Q' at turbine inlet and at exit of each blade row with uniform and nonuniform inlet conditions. At all stations, Q and Q' are greater with nonuniform inlet conditions than with uniform inlet conditions. For both inlet conditions, the nonuniformity at HP vane exit (station 2) is greater than that at turbine inlet (true for both metrics), suggesting that the introduction of vane coolant increases the total temperature nonuniformity at vane exit. The increase in parameter Q across the HP vane is unsurprising, given that the effect of coolant introduction is to lower the mass-mean total temperature while hot gas near mid-passage experiences relatively little mixing through the vane. The increase in parameter Q' across the HP vane with nonuniform inlet conditions indicates that the expected reduction in temperature nonuniformity due to mixing in the vane is outweighed by the nonuniformity introduced by the vane coolant injection.

At rotor exit (station 3), both Q and Q' are greater with nonuniform inlet conditions than with uniform inlet conditions. Comparing values at stations 2 and 3, however, shows that across the rotor, Q increases while Q' decreases. The Q increase reflects the persistence of local temperature peaks across the rotor: the T_0^{\max} reduction (due to work extraction and mixing) is smaller than the \bar{T}_0 reduction (due to work extraction alone). The Q' decrease reflects the overall flattening of the temperature nonuniformity due to work extraction and mixing across the rotor.

Across the IP vane, both Q and Q' are reduced (due to mixing) for both inlet conditions. At IP vane exit (station 4), both Q and Q' are approximately twice as great with nonuniform inlet conditions than with uniform inlet conditions. This result has significant implications for IP rotor design. A downstream rotor designed for a uniform T_{04} profile at the correct mass-mean value (or even a nonuniform T_{04} profile predicted for uniform turbine inlet conditions)

may experience local over-heating and suboptimal aerodynamic performance.

While there is—in general—good agreement between the measured and predicted T_{04} contours, the predicted contours for both inlet conditions are significantly lower in absolute temperature (across most of the passage) than the measured contours (by up to 4% of \bar{T}_{01}). Furthermore, the radial gradient is greater in the predictions than in the measurements—this is perhaps clearer in the radial profiles shown in Fig. 30(a). Since these discrepancies are similar to those observed at rotor exit, it is likely that this is, at least in part, due to failure of the URANS model to accurately predict the complex changes to the HP stage aerodynamics (the IP vane is adiabatic).

Figure 29(b) shows measured and predicted p_4 contours. For uniform inlet conditions, the measured and predicted contours both show a radial gradient increasing from hub to casing (due to the duct curvature in the meridional plane and reinforced by the flow turning of the vane) and a degree of circumferential nonuniformity (due to the IP vane potential field). Furthermore, both the measured and predicted contours show little difference due to the change in inlet conditions. There is disagreement, however, between the strengths of the measured and predicted radial pressure gradients. This discrepancy is more apparent in the corresponding radial profiles—see Fig. 30(b). The weaker pressure gradient in the measurements could be explained by a hub flow separation occurring in the experiment (a relatively common problem in highly whirling flows in hatched ducts) but not in the prediction; however, the lack of a substantial difference in total pressure loss near the hub suggests this is unlikely. Alternatively, the discrepancy could be due to an inaccuracy in the CFD outflow BC, which (as discussed in the Numerical Setup section) was set 0.6 IP vane axial chords downstream of the traverse plane using an assumed linearly varying profile between the measured hub and casing pressures at the same axial location. The traverse measurements near

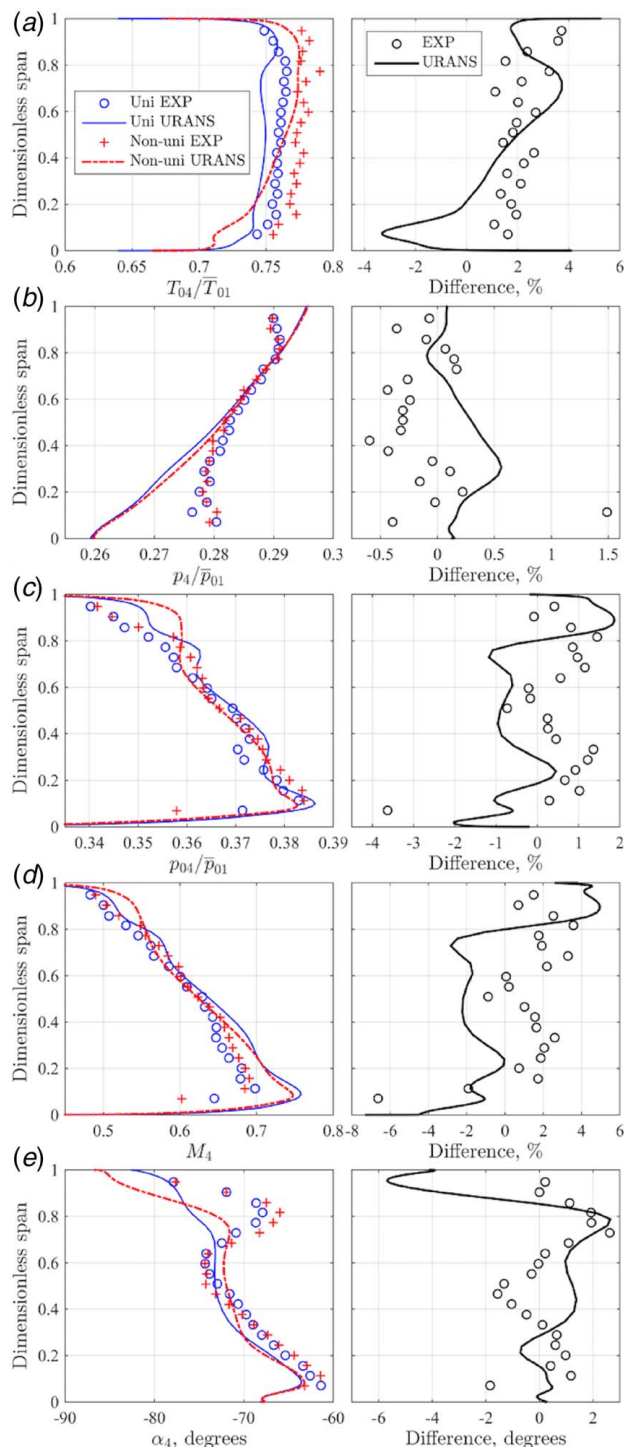


Fig. 30 Measured and time-averaged predicted radial profiles at the IP vane exit traverse plane: (a) total temperature, (b) static pressure, (c) total pressure, (d) Mach number, and (e) yaw angle. Results are shown for uniform and nonuniform inlet conditions (left), as are the differences with nonuniform inlet (right).

the endwalls (where discrepancy is greatest) may also be affected to a degree by the disturbance of the probe (interaction with the wall). A further potential explanation is that the measurements and CFD outflow BC are correct but the predicted flow in the vane—heavily affected by secondary flows—is poorly captured by the URANS model. This possibility is revisited later, after examining the p_{04} , M_4 , and α_4 contours.

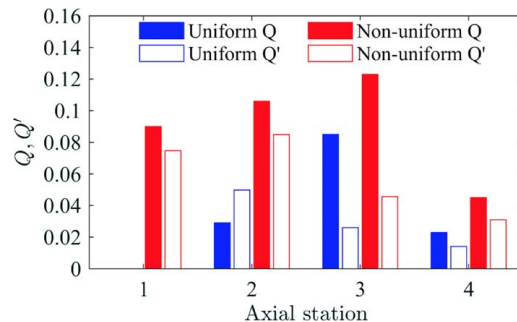


Fig. 31 Values of the global total temperature nonuniformity parameters at four stations through the turbine (based on time-averaged URANS solutions)

Figure 29(c) shows measured and predicted p_{04} contours. Corresponding radial profiles are shown in Fig. 30(c). The measurements and predictions are in good agreement in terms of both global levels and general distributions. The contours are characterized by a radial gradient decreasing from hub to casing (as primarily dictated by the rotor radial work distribution), a region of high-total pressure core flow, and streaks of slightly elevated total pressure near 80% span. In the predicted contours, twin loss cores are observed at the hub (outside the radial range covered by the measurements); these appear to be associated with two streamwise vortices observable in the predicted hub surface streamlines—see Fig. 28. With nonuniform inlet conditions, the changes to the p_{04} contours are small and complex. Most notable is a measured increase in level of the high total pressure streak near 80% span, which is also observed in the predictions, although at a slightly different location (near 90% span). This is clearer in the radial profiles—see Fig. 30(c)—and is likely due to the increase in total pressure near the casing at IP vane inlet—see Fig. 25(c).

Figure 29(d) shows measured and predicted M_4 contours. The contours are in good agreement. In particular, both show local peaks corresponding to the peaks in total pressure, as well as the loss cores discussed above. The measured and predicted contours also show a radial gradient increasing from hub to casing, although the predicted gradient is stronger than in the measurements (in particular below mid-span). This discrepancy is observed more clearly in the radial profiles—see Fig. 30(d)—and is associated with the greater predicted static pressure gradient (discussed previously).

Figure 29(e) shows measured and predicted contours of yaw angle, α_4 , at the IP vane exit plane. Below approximately mid-span, the measured and predicted contours are in good agreement in terms of the general distributions: both show similar localized regions of under-turned flow near the hub and well-matched radial profiles—see Fig. 30(e)—although the predicted turning below approximately 40% span is greater than in the experiment (by up to 3 deg). Above mid-span, there are larger differences between the measured and predicted profiles. The measurements show a local minimum in turning at approximately 80% span, which is approximately 6 deg below the predicted turning at the same span location.

We now attempt to reconcile the measured and predicted p_4 , p_{04} , M_4 , and α_4 profiles. First, consider the region below mid-span. There is around 3 deg greater turning in the prediction than in the measurements. Although this is a relatively small absolute difference, because the flow is strongly swirling (mean angle of around 70 deg) an increase in whirl angle would imply an attendant increase in acceleration. Increased whirl angle and increased velocity would both act to strengthen the radial static pressure gradient, causing lower static pressure toward the hub. The differences between the measured and predicted p_{04} profiles below mid-span are relatively small. Thus, the greater whirl angle in the prediction (compared with the measurement) and the attendant acceleration and static pressure drop provide the primary explanation (i.e.,

the effect is not driven by differences in total pressure) for greater M_4 below mid-span in the prediction compared with the measurements.

Now consider the near-casing region above approximately 75% span. The predicted turning (with associated acceleration) is again greater than in the experiment, causing a stronger radial static pressure gradient (with pressure increasing toward the casing). In contrast to the hub region, only a small difference between the measured and predicted M_4 profiles is observed near the casing. This is explained by greater local p_{04} in the predictions, which acts to offset the lower local p_4 in the predictions, leading to little difference in the predicted and measured M_4 profiles.

The differences between measurements and predictions discussed above highlight the limitations of the URANS model in capturing the highly complex flow in the IP vane. Flows in vanes with high hade angle and duct diffusion are well known to be dominated by large secondary flows. These have a steady component and a component that interacts in an unsteady manner with the outflow of the upstream stage (see Ref. [39], for example). Some significant differences between predictions and experiments are therefore unsurprising (see also, for example, Ref. [21]). More accurate prediction of the effects of lean-burn inlet conditions on the IP vane flow would likely require highly accurate BCs (often impossible in practice, where the accuracy extends to unsteady components, for example) or higher fidelity numerical methods (computationally impractical for full-stage analysis).

Conclusions

A detailed experimental and computational investigation of the impact of a representative lean-burn combustor exit profile on the aerodynamics of a 1.5-stage film-cooled turbine was conducted. Experiments were conducted in a transonic rotating turbine facility, which was recently upgraded with a new nonreacting lean-burn combustor simulator producing both swirl and hot-streak profiles at turbine inlet. To the authors' knowledge, this is the first study, including both experimental and computational results, of a rotating turbine with both of these inlet nonuniformities simulated simultaneously.

Changes to the HP vane aerodynamics were predominantly driven by the inlet swirl profile. These included a slight redistribution of loss from above to below mid-span and a redistribution of film coolant (which accumulated at some locations and dissipated at others). The vane exit flow was characterized by a pronounced radial total temperature nonuniformity (the inlet profile after only a small degree of modification by the vane flow) superimposed with a circumferential total temperature nonuniformity of comparable magnitude (due to the film-cooled HP vane wakes), and only a small amount of residual swirl.

Changes to the rotor aerodynamics were predominantly driven by the inlet total temperature profile. The radial temperature nonuniformity caused reduced time-mean local incidence angles near the endwalls that were of significantly greater magnitude (up to -12.7 deg) than the changes in incidence angles due to residual swirl at vane exit (± 1.5 deg). These reductions in incidence angle caused local reductions in blade loading (most significantly near the hub), and possibly a reduction in tip leakage flow: the tip leakage vortex size and loss were predicted to decrease. Near mid-span, the gas temperature was not significantly elevated (as a result of the mass-mean total temperature at turbine inlet being not exactly matched between uniform/nonuniform inlet testing), thus the time-mean off-design incidence angles near mid-span were small compared with near the endwalls. Both measurements and predictions indicated that the total temperature nonuniformity was preserved to a considerable degree during convection through the HP stage.

The IP vane aerodynamics was affected to a smaller, yet still significant degree. In particular, the vane loading and secondary flow structure were altered and a pronounced total temperature nonuniformity persisted at exit. While generally good agreement was

found between measurement and CFD prediction, the results highlighted challenges in modeling the complex flow in the highly haded and diffusing intermediate turbine duct and IP vane.

In summary, the results of this study support the conclusion (which is also supported by previous research) that HP vane aerodynamics is primarily affected by residual combustor swirl, while rotor aerodynamics is primarily affected by the inlet temperature nonuniformity. The results also suggest that these changes to the HP stage aerodynamics can have significant design implications for IP stage design.

Acknowledgment

The authors would like to acknowledge the financial support provided by the European Commission and its partners through the LEMCOTEC project (EU Grant No. 283216) within the Seventh Framework Programme and that provided by Rolls-Royce plc. The authors would also like to thank D. N. Cardwell and S. Chana of the University of Oxford for their assistance in running the test facility, and B. F. Hall and T. Godfrey, also of the University of Oxford, for their assistance in designing and constructing the instrumentation, respectively.

Conflict of Interest

There are no conflicts of interest.

Data Availability Statement

The authors attest that all data for this study are included in the paper. Data provided by a third party listed in Acknowledgment.

Nomenclature

p	= pressure, bar
r	= radial coordinate, m
x	= axial coordinate, m
M	= Mach number
N	= rotational speed, rpm
Q	= first global total temperature nonuniformity parameter, $(T_0^{max} - T_0)/\bar{T}_0$
R	= specific gas constant, J/(kg K)
T	= temperature, K
U	= rotor blade speed, m/s
\dot{m}	= mass flowrate, kg/s
C_{ax}	= vane/blade axial chord, m (at mid-span unless otherwise stated)
C_{p0}	= total pressure loss coefficient, $(\bar{p}_{01} - p_0)/((\bar{p}_{01} - \bar{p}_2))$
Q'	= second global total temperature nonuniformity parameter, $\text{rms}(T_0 - \bar{T}_0)/\bar{T}_0$
Re	= Reynolds number
Re _{HPV}	= Reynolds number based on HP vane axial chord at mid-span

Greek Symbols

α	= absolute yaw angle, degrees (positive in direction of HP rotor blade motion)
Γ	= capacity, $\text{kg s}^{-1} \text{K}^{1/2} \text{Pa}^{-1}$
ε	= nondimensional total temperature effectiveness, $(T_0 - T_{0c})/(T_{0h} - T_{0c})$

Subscripts

c	= cold stream/coolant
h	= hot stream
rel	= relative
θ	= tangential component

- 0 = gas stagnation condition
- 1 = turbine inlet
- 2 = HP vane exit
- 3 = HP rotor exit
- 4 = IP vane exit

Superscripts and Annotations

- $\overline{[]}$ = average (mass flow-weighted unless otherwise stated)
- $[\]^{circ}$ = circumferential profile (radially averaged)
- $[\]^{radial}$ = radial profile (circumferentially averaged)

Abbreviations

- 2D/3D = two/three-dimensional
- EXP = experiment
- LEMCOTEC = low-emissions core engine technologies
- S1 = HP vane with LE *aligned* (at mid-span) with swirler centerline
- S2 = HP vane with LE *misaligned* (at mid-span) with swirler centerline

References

- [1] Munk, M., and Prim, R., 1947, "On the Multiplicity of Steady Gas Flows Having the Same Streamline Pattern," *Proc. Natl. Acad. Sci. U. S. A.*, **33**(5), pp. 137–141.
- [2] Butler, T. L., Sharma, O. P., Joslyn, H. D., and Dring, R. P., 1989, "Redistribution of an Inlet Temperature Distortion in an Axial Flow Turbine Stage," *J. Propul. Power*, **5**(1), pp. 64–71.
- [3] Beard, P. F., Smith, A. D., and Povey, T., 2013, "Impact of Severe Temperature Distortion on Turbine Efficiency," *ASME J. Turbomach.*, **135**(1), p. 011018.
- [4] Kerrebrock, J. L., and Mikolajczak, A. A., 1970, "Intra-Stator Transport of Rotor Wakes and its Effect on Compressor Performance," *J. Eng. Power*, **92**(4), pp. 359–368.
- [5] Prasad, D., and Hendricks, G. J., 2000, "A Numerical Study of Secondary Flow in Axial Turbines With Application to Radial Transport of hot Streaks," *ASME J. Turbomach.*, **122**(4), pp. 667–673.
- [6] Hawthorne, W. R., 1951, "Secondary Circulation in Fluid Flow," *Proc. R. Soc. London, Ser. A*, **206**(1086), pp. 374–387.
- [7] Shang, T., and Epstein, A. H., 1997, "Analysis of hot Streak Effects on Turbine Rotor Heat Load," *ASME J. Turbomach.*, **119**(3), pp. 544–553.
- [8] Povey, T., Chana, K. S., and Jones, T. V., 2003, "Heat Transfer Measurements on an Intermediate-Pressure Nozzle Guide Vane Tested in a Rotating Annular Turbine Facility, and the Modifying Effects of a Non-Uniform Inlet Temperature Profile," *Proc. Inst. Mech. Eng., Part A*, **217**(4), pp. 421–431.
- [9] Chana, K. S., and Jones, T. V., 2003, "An Investigation on Turbine Tip and Shroud Heat Transfer," *ASME J. Turbomach.*, **125**(3), pp. 513–520.
- [10] Povey, T., Chana, K. S., Jones, T. V., and Hurron, J., 2007, "The Effect of Hot-Streaks on HP Vane Surface and Endwall Heat Transfer: An Experimental and Numerical Study," *ASME J. Turbomach.*, **129**(1), pp. 32–43.
- [11] Qureshi, I., Smith, A. D., Chana, K. S., and Povey, T., 2012, "Effect of Temperature Nonuniformity on Heat Transfer in an Unshrouded Transonic HP Turbine: An Experimental and Computational Investigation," *ASME J. Turbomach.*, **134**(1), p. 011005.
- [12] Salvadori, S., Montomoli, F., Martelli, F., Adami, P., Chana, K. S., and Castillon, L., 2011, "Aerothermal Study of the Unsteady Flow Field in a Transonic Gas Turbine With Inlet Temperature Distortions," *ASME J. Turbomach.*, **133**(3), p. 031030.
- [13] Simone, S., Montomoli, F., Martelli, F., Chana, K. S., Qureshi, I., and Povey, T., 2012, "Analysis on the Effect of a Nonuniform Inlet Profile on Heat Transfer and Fluid Flow in Turbine Stages," *ASME J. Turbomach.*, **134**(1), p. 011012.
- [14] Chana, K. S., Hurron, J. R., and Jones, T. V., "The Design, Development and Testing of a Nonuniform Inlet Temperature Generator for the QinetiQ Transient Turbine Research Facility," ASME Paper No. GT2003-38469.
- [15] Povey, T., and Qureshi, I., 2008, "A Hot-Streak (Combustor) Simulator Suited to Aerodynamic Performance Measurements," *Proc. Inst. Mech. Eng., Part G*, **222**(6), pp. 705–720.
- [16] Povey, T., and Qureshi, I., 2009, "Developments in Hot-Streak Simulators for Turbine Testing," *ASME J. Turbomach.*, **131**(3), p. 031009.
- [17] Qureshi, M. I., and Povey, T., 2011, "A Combustor-Representative Swirl Simulator for a Transonic Turbine Research Facility," *Proc. Inst. Mech. Eng., Part G*, **225**(7), pp. 737–748.
- [18] Qureshi, I., Smith, A. D., and Povey, T., 2013, "HP Vane Aerodynamics and Heat Transfer in the Presence of Aggressive Inlet Swirl," *ASME J. Turbomach.*, **135**(2), p. 021040.
- [19] Qureshi, I., Beretta, A., Chana, K., and Povey, T., 2012, "Effect of Aggressive Inlet Swirl on Heat Transfer and Aerodynamics in an Unshrouded Transonic HP Turbine," *ASME J. Turbomach.*, **134**(6), p. 061023.
- [20] Beard, P. F., Smith, A. D., and Povey, T., 2014, "Effect of Combustor Swirl on Transonic High Pressure Turbine Efficiency," *ASME J. Turbomach.*, **136**(1), p. 011002.
- [21] Johansson, M., Povey, T., Chana, K. S., and Abrahamsson, H., 2017, "Effect of Low-NOx Combustor Swirl Clocking on Intermediate Turbine Duct Vane Aerodynamics With an Upstream High Pressure Turbine Stage—An Experimental and Computational Study," *ASME J. Turbomach.*, **139**(1), p. 011006.
- [22] Werschnik, H., Schiffer, H. P., and Steinhausen, C., 2017, "Robustness of a Turbine Endwall Film Cooling Design to Swirling Combustor Inflow," *J. Propul. Power*, **33**(4), pp. 917–926.
- [23] Werschnik, H., Schneider, M., Herrmann, J., Ivanov, D., Schiffer, H. P., and Lyko, C., 2017, "The Influence of Combustor Swirl on Pressure Losses and the Propagation of Coolant Flows at the Large Scale Turbine Rig (LSTR): Experimental and Numerical Investigation," *Int. J. Turbomach. Propuls. Power*, **2**(3), p. 12.
- [24] Jacobi, S., Mazzoni, C., Rosic, B., and Chana, K., 2017, "Investigation of Unsteady Flow Phenomena in First Vane Caused by Combustor Flow With Swirl," *ASME J. Turbomach.*, **139**(1), p. 041006.
- [25] Koupper, C., Caciolli, G., Gicquel, L., Duchaine, F., Bonneau, G., Tarchi, L., and Facchini, B., 2014, "Development of an Engine Representative Combustor Simulator Dedicated to Hot-Streak Generation," *ASME J. Turbomach.*, **136**(11), p. 111007.
- [26] Bacci, T., Becchi, R., Picchi, A., and Facchini, B., 2019, "Adiabatic Effectiveness on High-Pressure Turbine Nozzle Guide Vanes Under Realistic Swirling Conditions," *ASME J. Turbomach.*, **141**(1), p. 011008.
- [27] Khanal, B., He, L., Northall, J., and Adami, P., 2013, "Analysis of Radial Migration of Hot-Streak in Swirling Flow Through High-Pressure Turbine Stage," *ASME J. Turbomach.*, **135**(4), p. 041005.
- [28] Rahim, A., and He, L., 2015, "Rotor Blade Heat Transfer of High Pressure Turbine Stage Under Inlet Hot-Streak and Swirl," *ASME J. Eng. Gas Turbines Power*, **137**(6), p. 062601.
- [29] Bacci, T., Lenzi, T., Picchi, A., Mazzei, L., and Facchini, B., 2019, "Flow Field and Hot Streak Migration Through a High Pressure Cooled Vanes With Representative Lean Burn Combustor Outflow," *ASME J. Eng. Gas Turbines Power*, **141**(4), p. 041020.
- [30] Hilditch, M. A., Fowler, A., Jones, T. V., Chana, K. S., Oldfield, M. L. G., Ainsworth, R. W., Hogg, S. I., Anderson, S. J., and Smith, G. C., 1994, "Installation of a Turbine Stage in the Pyestock Isentropic Light Piston Facility," ASME Paper No. 94-GT-277.
- [31] Beard, P. F., Adams, M. G., Stokes, M. R., Wallin, F., Cardwell, D. N., Povey, T., and Chana, K. S., 2019, "The LEMCOTEC 1½ Stage Film-Cooled HP Turbine: Design, Integration, and Testing in the Oxford Turbine Research Facility," Proceedings of the 13th European Conference on Turbomachinery Fluid Dynamics and Thermodynamics, Lausanne, Switzerland, Apr. 7–12.
- [32] Hall, B. F., Chana, K. S., and Povey, T., 2014, "Design of a Non-Reacting Combustor Simulator With Swirl and Temperature Distortion With Experimental Validation," *ASME J. Eng. Gas Turbines Power*, **136**(8), p. 081501.
- [33] Hall, B. F., and Povey, T., 2015, "Experimental Study of Non-Reacting Low NOx Combustor Simulator for Scaled Turbine Experiments," ASME Paper No. GT2015-43530.
- [34] Adams, M. G., Povey, T., Hall, B. F., Cardwell, D. N., Chana, K. S., and Beard, P. F., 2020, "Commissioning of a Combined Hot-Streak and Swirl Profile Generator in a Transonic Turbine Test Facility," *ASME J. Eng. Gas Turbines Power*, **142**(3), p. 031008.
- [35] Hall, B. F., 2015, "Combustor Simulators for Scaled Turbine Experiments," D.Phil. thesis, University of Oxford.
- [36] Nagawkar, J. R., 2016, "Unsteady 3D CFD Analysis of a Film-Cooled 1½ Stage Turbine," M.Sc. thesis, Chalmers University of Technology.
- [37] Perdichizzi, A., and Dossena, V., 1992, "Incidence Angle and Pitch-Chord Effects on Secondary Flows Downstream of a Turbine Cascade," ASME Paper 92-GT-184.
- [38] Lim, C. H., Pullan, G., and Northall, J., 2012, "Estimating the Loss Associated With Film Cooling for a Turbine Stage," *ASME J. Turbomach.*, **134**(2), p. 021011.
- [39] Miller, R. J., Moss, R. W., Ainsworth, R. W., and Harvey, N. W., 2004, "The Effect of an Upstream Turbine on a Low-Aspect Ratio Vane," ASME Paper No. GT2004-54017.